

Probing Radiative Neutrino Mass Generation through Monotop Production

John N. Ng and Alejandro de la Puente

Theory Group, TRIUMF, Vancouver BC V6T 2A3, Canada

(Dated: November 27, 2019)

We present a generalization of a model where the right-handed up-type quarks serve as messengers for neutrino mass generation and as a portal for dark matter. Within this framework the Standard Model is extended with a single Majorana neutrino, a coloured electroweak-singlet scalar and a coloured electroweak-triplet scalar. We calculate the relic abundance of dark matter and show that we can match the latest experimental results. Furthermore, the implications from the scattering between nuclei and the dark matter candidate are studied and we implement the latest experimental constraints arising from flavour changing interactions, Higgs production and decay and LHC collider searches for a single jet and jets plus missing energy. In addition, we implement constraints arising from scalar top quark pair-production. We also study the production of a single top in association with missing energy and calculate the sensitivity of the LHC to the top quark hadronic and semi-leptonic decay modes with the current 20 fb^{-1} data set at a centre of mass energy of $\sqrt{s} = 8 \text{ TeV}$. Furthermore, we carry out the analysis to centre of mass energies of $\sqrt{s} = 14 \text{ TeV}$ with 30 and 300 fb^{-1} of data.

I. INTRODUCTION

We now have ample evidence pointing towards the existence of dark matter [1, 2]. Gravitational phenomena such as velocity dispersion and rotation curves of galaxies suggest the existence of non-luminous matter not composed of the known Standard Model (SM) particles [3, 4]. The most recent data from the Planck collaboration, which builds upon the successful findings of WMAP [5], estimates a cold dark matter cosmological parameter $\Omega_{\text{DM}}h^2 = 0.1199 \pm 0.0027$ [6]. However, due to the solely gravitational evidence regarding the existence of dark matter, its identity remains unknown. One candidate explanation for dark matter is the existence of a weakly interacting massive particle (WIMP). Models of beyond the SM physics such as the Minimal Supersymmetric Standard Model (MSSM) provide a natural WIMP and reproduce the right abundance in the universe determined by their self-annihilation rate. Furthermore, WIMPs may scatter off nuclei in direct detection experiments, and one can probe the spin dependent [7–11] and spin independent scattering cross sections [12–15]. These experiments, together with the relic abundance of dark matter in the universe provide stringent constraints on models beyond the SM with a WIMP candidate.

With the LHC running, scales beyond the electroweak scale are now being probed. The search for new particles and interactions is now underway. In particular, searching for collider signatures that may point at the nature of dark matter has become an active program by both the CMS and ATLAS collaborations. Current dark matter searches are usually carried out by analyzing the possibility that jets are produced in association with a large amount of missing transverse energy (MET) [16–19]. Furthermore, final states that do not appear in the SM at tree level have been proposed in order to enhance the sensitivity to dark matter production. One such final state was proposed in [20], where a single top quark is produced in association with MET. This final state, in analogy to its light-quark analogue (monojet), has been named monotop. Monotop production provides a signal that is easier to discriminate than monojet production since the top quark fixes the flavour in the final state. The CDF collaboration carried out a search with 7.7 fb^{-1} of data at 1.96 TeV centre of mass energies [21]. They were able to set 95% confidence level upper limits on the cross section for the process $p\bar{p} \rightarrow t + \text{MET}$. Models beyond the SM with a monotop signature have been proposed and in particular models where an effective theory approach has been taken have analyzed the significance of a signal in both the hadronic and semi-leptonic decay modes of the top quark with the 7 and 8 TeV data sets at the LHC [20, 22, 23]. Top-down approaches have also been studied. In particular, a charged Z' model was proposed to address the non-zero forward-backward top asymmetry at the Tevatron and the null charge asymmetry at the LHC [24, 25]. A monotop signal can also arise within a Type II Two-Higgs doublet model supplemented with a SM gauge singlet scalar, identified as the dark matter candidate [26]. The significance of a monotop signal in the last two models has been analyzed in [28] and a future search by the LHC can probe the Z' model with the current 20 fb^{-1} of data at 8 TeV centre of mass energies. Another model implements a coloured electroweak-singlet scalar and three Majorana fermions, uncharged under the SM gauge symmetry, to address the non-zero forward-backward top asymmetry through on shell production of the coloured scalar [29]. Furthermore, supersymmetric models with R -parity violation can lead to singly produced top quarks in association with a long-lived neutralino [30–32]. In this work we revisit the model introduced in [33] where, without extending the SM gauge symmetry, we incorporate a Majorana neutrino coupling to up-type right-handed quarks through a coloured electroweak-singlet scalar. The simplest and most economical case studied there used only the top and charm quarks. In addition, we add a coloured electroweak-triplet scalar coupling to left-handed leptons and left-handed quarks. Our model belongs to a family of models where the dark matter relic abundance is induced by the exchange of a t -channel scalar mediator and where the dark matter nucleon scattering cross section is through the t -channel exchange of the mediator [34–38]. Furthermore, within our framework active neutrino masses are generated radiatively and can be understood in a generalized seesaw framework. The active neutrino masses are given by the effective $\frac{g_{eff}}{\Lambda}(LH)^2$ operator where the seesaw scale is Λ and g_{eff} is some effective coupling. For our model, $\Lambda \simeq O(\text{TeV})$, is determined by the mass of the heavy coloured scalar. The coupling g_{eff} is a product of 3 loop-factors, several Yukawa and scalar couplings of which the top Yukawa coupling is the largest. Hence, the top quark plays a very special role. In [33], the right-handed up quark was not coupled to the Majorana neutrino and the coloured electroweak-singlet and thus we were able to easily evade most dark matter direct detection constraints and current monojet and jets + MET constraints at the LHC. Similarly within that framework, new collider signatures that can be probed with current and future data, such as monotops, were also absent. Making the up quark play an active role not only completes the model but also provides us with a clear monotop signature that would have been suppressed in the previous simplified model. It would be interesting to witness future analyses by the CMS and ATLAS collaborations that can probe models such as ours that predict the production of a singlet top quark in association with a dark matter particle. In our case, this could be evidence of the underlying mechanism that bestows neutrinos with mass.

The summary of our study is as follows: In Section II we review the model and in Section III the mechanism that leads to the relic abundance of dark matter. Furthermore, we analyze the implications from the scattering between nuclei and our dark matter candidate. In Section IV we review the mechanism that radiatively generates active neutrino masses. In Section V we analyze all of the experimental constraints sensitive to our framework and

in Section VI we summarize our results and present the allowed regions of parameter space within different model scenarios. In Section VII we analyze the monotop signal that arises in our framework and discuss the sensitivity of the LHC to the top quark hadronic and semi-leptonic decay modes with the current 20 fb⁻¹ data set at 8 TeV centre of mass energies. We then carry out an analysis of the future sensitivity at 14 TeV LHC and conclude in Section VIII.

II. THE BASIC MODEL

Within this framework, without extending the SM gauge symmetry, we incorporate a Majorana neutrino, N_R , that couples to right-handed up-type quarks through a coloured electroweak-singlet scalar, ψ transforming as a $(\mathbf{3}, \mathbf{1}, \mathbf{2}/\mathbf{3})$ under the SM gauge group. We also introduce couplings between left-handed leptons and left-handed quarks through a coloured electroweak-triplet, χ

$$\chi = \begin{pmatrix} \chi_2/\sqrt{2} & \chi_1 \\ \chi_3 & -\chi_2/\sqrt{2} \end{pmatrix}, \quad (1)$$

transforming as a $(\mathbf{3}, \mathbf{3}, -\mathbf{1}/\mathbf{3})$ under the SM gauge group. The new operators are parametrized by the following Lagrangian:

$$-\mathcal{L}_{BSM} = \sum_i y_\psi^i \bar{u}^i P_L N^c \psi + \sum_{\ell, i} \left\{ \lambda_\ell^i [\bar{u}^i P_R (\chi_1 \nu_\ell^c + \chi_2 \ell^c) + \bar{d}^i P_R (\chi_3 \ell^c - \chi_2 \nu_\ell^c)] \right\} + \text{hc}, \quad (2)$$

where $l = e, \mu, \tau$ and $i = 1, 2, 3$ is the quark family index. Also P_L and P_R are the left- and right-handed projection operators. The coupling y_ψ^i denotes the strength of the interaction between N_R and u_R^i via ψ , while λ_ℓ^i denotes the strength between the quark doublets $(u^i, d^i)_L$ and lepton $(\nu, l)_L$ via χ .

Within this model we also incorporate an arbitrary mass parameter for the Majorana neutrino, M_{N_R} , in the Lagrangian and introduce a Z_2 parity, denoted dark parity (DP), into the model. We let N_R and ψ be odd under it, with all other fields transforming evenly under it. This assignment is useful since it will allow us to identify N_R with a dark matter candidate for $M_{N_R} < m_\psi$. Throughout this work we take $m_\psi > M_{N_R}$ and parametrize the mass term for N_R with the usual Majorana mass $\frac{1}{2} M_N \bar{N}_R^c N_R$.

We also introduce the most general gauge and Z_2 symmetric scalar Lagrangian:

$$\begin{aligned} V(H, \psi, \chi) = & -\mu^2 H^\dagger H + \frac{\lambda}{4!} (H^\dagger H)^2 + m_\chi^2 \text{Tr}(\chi^\dagger \chi) + \lambda_\chi (\text{Tr} \chi^\dagger \chi)^2 \\ & + m_\psi^2 \psi^\dagger \psi + \lambda_\psi (\psi^\dagger \psi)^2 + \kappa_1 H^\dagger H \text{Tr} \chi^\dagger \chi + \kappa_2 H^\dagger \chi^\dagger \chi H \\ & + \kappa_3 H^\dagger H \psi^\dagger \psi + \rho_1 (\text{Tr} \chi^\dagger \chi) \psi^\dagger \psi, \end{aligned} \quad (3)$$

where H is the SM Higgs field. We emphasize that in order to avoid a colour breaking vacuum, m_χ^2 and m_ψ^2 must be positive. Furthermore, one can see that in this framework, the Z_2 dark parity remains exact after electroweak symmetry breaking.

III. DARK MATTER

A. Relic Abundance

The existence of an unbroken Z_2 symmetry stabilizes N_R and the nature of the Lagrangian introduced in Equation (2) yields a mechanism for its relic abundance. This mechanism is the N_R pair annihilation through a t - and u -channel exchange of the new coloured electroweak-singlet, ψ . The u -channel is available because N_R has similar properties as a Majorana fermion. These diagrams are depicted in Figure 1.

The present day relic abundance is given by [39]

$$\Omega_{DM} h^2 \approx 1.65 \times 10^{-10} \left(\frac{\text{GeV}^{-2}}{\langle \sigma v \rangle} \right) \log \left(0.038 g \frac{m_{Pl} \langle \sigma v \rangle}{g_*^{1/2}} \right), \quad (4)$$

where we have dropped the temperature dependence in the logarithm since it is not an important factor in the region we are studying. The most important controlling factor above is $\langle \sigma v \rangle$ and the correct relic abundance can be achieved with a value of $\langle \sigma v \rangle \simeq 3 \times 10^{-26} \text{ cm}^3/\text{s}$.

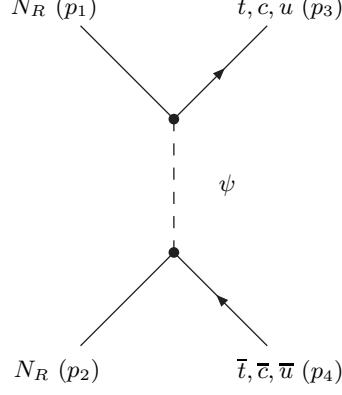


FIG. 1. Interaction channels that lead to a reduction in the relic abundance of N_R : Channels consist of annihilation into $u_i \bar{u}_j$, $i, j = u, c, t$. A similar u -channel graph is not shown.

The thermalized cross section at temperature T can be calculated from the annihilation cross section of our dark matter candidate, N_R . The annihilation channels are depicted in Figure 1. The thermalized cross section is given by

$$\langle \sigma_{N_R N_R} v \rangle = \int_{4M_{N_R}^2}^{\infty} ds \frac{(s - 4M_{N_R}^2) s^{1/2} K_1(s^{1/2}/T)}{8M_{N_R}^4 T K_2^2(M_{N_R}/T)} \sigma(s), \quad (5)$$

where $\sigma(s)$ is the annihilation cross section of the $2 \rightarrow 2$ annihilation process

$$\frac{d\sigma(s)}{d\Omega} = \frac{|M|^2}{64\pi^2 s} \frac{|\vec{p}_3|}{|\vec{p}_1|}, \quad (6)$$

and $K_1(z), K_2(z)$ are Modified Bessel functions of the first and second kind respectively. This procedure requires elaborate numerical computations. Below we outline a good approximate calculation of σv which we check against the numerical calculations.

In our analysis we use the Boltzmann distribution to calculate the thermal averaged cross section. This allows us to consider a low velocity expansion of the annihilation cross section:

$$\sigma v_{rel} \approx a_{rel} + b_{rel} v_{rel}^2 + \dots, \quad (7)$$

where v_{rel} is related to the center of mass velocity of the annihilating particle by $v_{CM} = v_{rel}/2$. We also make use of a technique studied in [40] which uses the fact that Mandelstam variables can be expanded in the following way

$$\begin{aligned} s &= s_0 + s_2 v_{CM}^2 + \dots + \\ t &= t_0 + t_1 \cos \theta v_{CM} + t_2 v_{CM}^2 + \dots + \end{aligned} \quad (8)$$

With this in mind, and using the notations of [40], the differential cross section can be written as

$$v_{cm} \frac{d\sigma(s)}{d\Omega} = \frac{J(s, t)}{4\pi} K(s) \sqrt{1 - v_{cm}^2}, \quad (9)$$

where $J(s, t) = |M|^2$ and $K(s) = |\vec{p}_3|/16\pi m s$ can both be expanded about $s = s_0$ and $t = t_0$ to obtain

$$\begin{aligned} a_{rel} &= 2J_0 K_0 \\ b_{rel} &= \frac{1}{2} J_0 K_2 - \frac{1}{4} J_0 K_0 + \frac{1}{2} J_2 K_0. \end{aligned} \quad (10)$$

For annihilation only into light quarks, the thermalized cross section is p -wave suppressed and it is given by

$$\langle \sigma_{N_R N_R} v \rangle \approx v_{rel}^2 \left[(y_\psi^u)^4 + (y_\psi^c)^4 \right] \frac{m_{N_R}^2 (m_{N_R}^4 + m_\psi^4)}{16\pi (m_{N_R}^2 + m_\psi^2)^4}, \quad (11)$$

while for annihilation mainly into $t\bar{t}$, small $y_\psi^{u,c}$, the thermalized cross section is dominated by the s -wave:

$$\begin{aligned} \langle \sigma_{N_R N_R v} \rangle \approx & \frac{3m_t^2 (y_\psi^t)^2}{128\pi M_{N_R}^4} \left(\frac{4(y_\psi^t)^2 M_{N_R}^3 \sqrt{(M_{N_R} - m_t)(M_{N_R} + m_t)}}{(M_{N_R}^2 - m_t^2 + m_\psi^2)^2} \right. \\ & \left. - \frac{[(y_\psi^u)^2 + (y_\psi^c)^2](4M_{N_R}^2 - m_t^2)^2}{2(2M_{N_R}^2 - m_t^2 + 2m_\psi^2)^2} \right). \end{aligned} \quad (12)$$

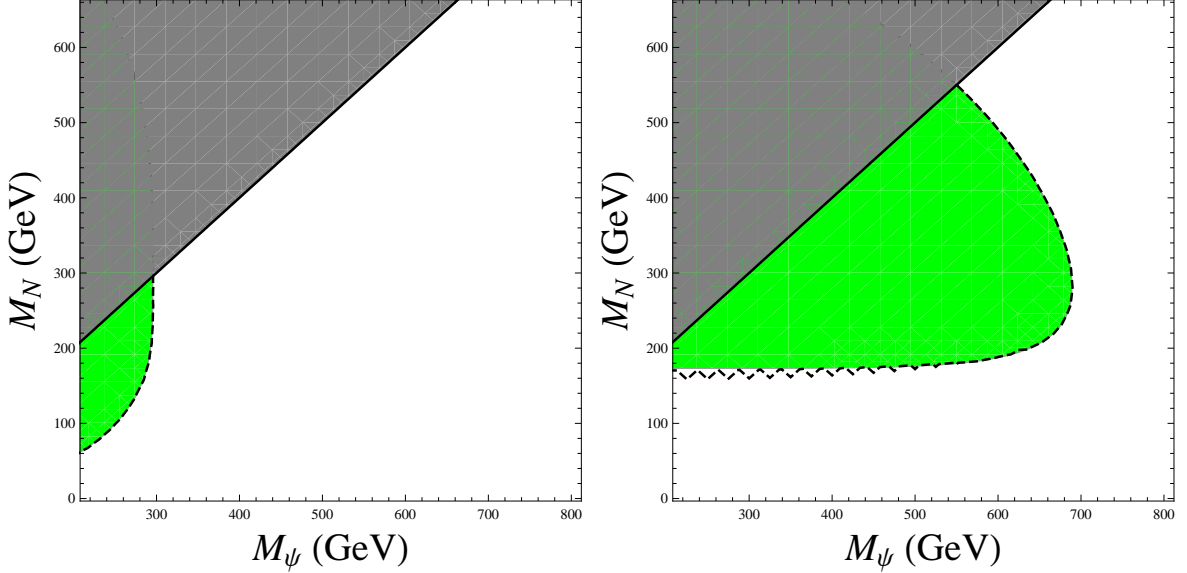


FIG. 2. Thermalized cross section in the $m_\psi - M_{N_R}$ plane for $y_\psi^{t,u} \approx 0$, $y_\psi^c = 1$ on the left and $y_\psi^{c,u} = 0$, $y_\psi^t = 1$ on the right. The green region corresponds to $\langle \sigma v \rangle > 3 \times 10^{-26} \text{ cm}^3/\text{s}$ while the dashed black line to $\langle \sigma v \rangle = 3 \times 10^{-26} \text{ cm}^3/\text{s}$.

With the above method, our calculations were in good agreement with the relic abundance generated by MicrOMEGAs [41] with model files generated with the latest version of FeynRules [42]. We would also like to emphasize that near the degenerate region, $M_{N_R} \approx m_\psi$, co-annihilation effects become important. The co-annihilation channels that contribute to the relic abundance calculation are $N_R \psi^\dagger \rightarrow u/c/t, g$ as well as the $\psi \psi^\dagger$ annihilation channels. These channels tend to make the annihilation process more efficient requiring lower values of $y_\psi^{t,c,u}$ and become important if the mass difference, $\delta m = m_\psi - M_{N_R}$, is small compared to the freeze-out temperature of the Majorana neutrino [43]. Within our framework, the region consistent with the cold dark matter cosmological parameter sits away from this region and thus co-annihilation effects can be safely neglected. The results for $y_\psi^{t,u} = 0$ and $y_\psi^c = 1$ are shown in Figure 2(a). The dashed line corresponds to an annihilation cross section of $\langle \sigma v \rangle = 3 \times 10^{-26} \text{ cm}^3/\text{s}$, the grey region corresponds to $m_\psi < M_{N_R}$ and the green region to an annihilation cross section into a pair of charm quarks greater than $3 \times 10^{-26} \text{ cm}^3/\text{s}$. For $y_\psi^t = 1$ and $y_\psi^{c,u} = 0$ the annihilation will be into $t\bar{t}$ and the s wave contribution dominates. We can see this in Figure 2(b) where the green region corresponds to s -wave contributions greater than $3 \times 10^{-26} \text{ cm}^3/\text{s}$.

B. Direct Detection

In our framework, the dark matter candidate is a Majorana fermion with chiral symmetric interactions that lead to a non-relativistic WIMP-nucleon scattering cross section dominated by spin-dependent interactions [44]. The scattering is dominated by t - and u -channel exchanges of the coloured electroweak-singlet, ψ . The amplitude in terms of the quark-current expectation values is given by

$$\mathcal{M} = \frac{1}{(m_\psi^2 - M_{N_R}^2)} \bar{u}_{N_R} \gamma^\mu \gamma^5 u_{N_R} \langle \bar{q} \gamma_\mu \gamma^5 q \rangle, \quad (13)$$

and the cross section by

$$\sigma_{SD}^N = \frac{3(y_\psi^u)^4 \Delta_N^2}{64\pi[(m_\psi^2 - M_{N_R}^2)^2 + \Gamma_\psi^2 m_\psi^2]} \frac{M_{N_R} m_N}{M_{N_R} + m_N}, \quad (14)$$

where $\Delta_{p(n)} = 0.78$ (-0.48) is the spin fraction of the proton (neutron) carried by the u -quark [45], m_N the mass of the nucleon, and Γ_ψ is the full width of the scalar mediator. The implications of the coupling between the u -quark and a Majorana fermion has recently been studied in [34–36]. However, in these works, the coloured electroweak-singlet couples only to the up -quark unlike our framework where it is free to couple to all three generations. Furthermore, the authors in [36] show that a spin-independent signal can be generated by the following effective operators:

$$\begin{aligned} O_1 &= \frac{\alpha_S}{4\pi} G^{a\mu\nu} G_{\mu\nu}^a N_R^2 \\ O_2 &= m_q \bar{q} q N_R^2, \end{aligned} \quad (15)$$

where $G_{\mu\nu}^a$ is the gluon field tensor and α_S is the strong coupling constant; but this signal is suppressed compared to the spin-dependent contribution given in Equation 14. Therefore, for a coupling to protons we compare our prediction to limits set by SIMPLE, COUPP and PICASSO [7–9] which set the most stringent constraints to date and limits from XENON10 [10] for the case where the Majorana neutrino couples to neutrons. The XENON100 results are now available [11] and we note that they are an order of magnitude stronger than those from XENON10 for dark matter masses above 10 GeV.

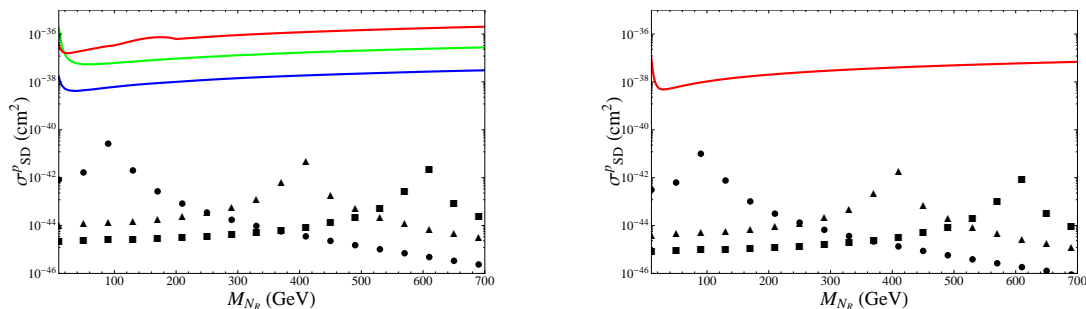


FIG. 3. Spin dependent cross section as a function of the Majorana neutrino mass, M_{N_R} for $y_\psi^u = 0.1$. For coupling to protons (left), limits from COUPP [7], PICASSO [8], and SIMPLE [9] are shown in green, red and blue respectively while the spin dependent cross section for scalar mediator masses of $m_\psi = 100, 400, 600$ GeV are depicted by the solid disks, triangles and squares respectively. For coupling to neutrons (right), limits from XENON10 [10] are shown in red.

In Figures 3(a) and 3(b) we show the spin dependent cross section as a function of the Majorana neutrino mass for coupling to the proton and the neutron respectively with $y_\psi^u = 0.1$. We have made use of DMTools [46] to plot the limits. In the figures we show the spin dependent cross section for three scalar mediator masses. The solid circles correspond to $m_\psi = 100$ GeV, while the solid triangles and squares correspond to $m_\psi = 400, 600$ GeV respectively. It is evident from the figures that the cross section is enhanced for $M_{N_R} \approx m_\psi$, but the corresponding coupling is too small to constrain the model. In Figures 4(a) and 4(b) we show the spin-dependent cross section with $y_\psi^u = 0.5$. Here we see that for small coloured electroweak-singlet mediator with mass ~ 100 GeV, the region where $m_\psi \sim M_{N_R}$ is excluded in both proton and neutron scattering. Therefore, direct detection constraints rule out well tuned combinations of couplings and masses as expected from Equation 14; and one may want to stay away from the resonant regions for $y_\psi^u \rightarrow 1$.

IV. RADIATIVE NEUTRINO MASS GENERATION

In [33] it is mentioned that the unbroken DP can be used to forbid Dirac neutrino mass terms for the active neutrinos, ν_i . Therefore, within this framework the usual seesaw mechanism is not operative. However, we showed that the Lagrangian of Equation (2) had enough structure to radiatively generate masses for ν_i via the exchange of the exotic coloured scalars. In particular, it had the novel feature of using the right-handed up-type quarks as a portal to communicate with the dark sector. Furthermore, the up-type quarks served as messengers to radiatively generate Majorana masses for the active neutrinos; with the lowest order diagram for neutrino mass generation at

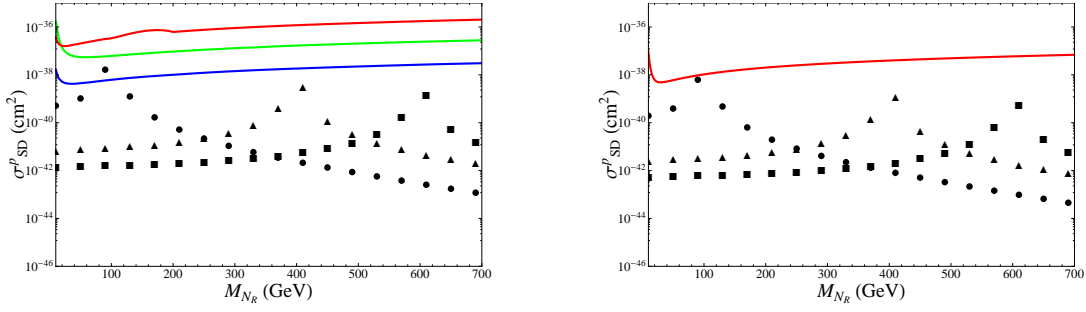


FIG. 4. Same as in Figure 3(a) and 3(b) but with $y_\psi^u = 0.5$

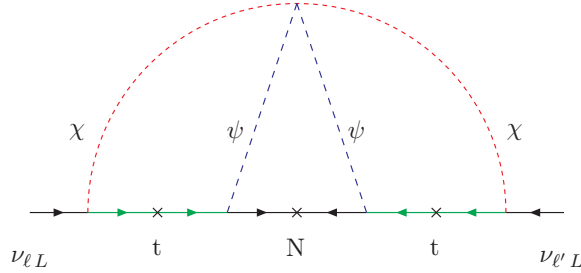


FIG. 5. 3-loop generation of a Majorana mass for active neutrinos from the t-quark. The crosses on the fermion lines indicate mass insertions. Similar diagrams from the u - and c -quarks will also play a role.

three-loops. Models where neutrino masses are generated at the three-loop level have been studied in the past. In particular, the model proposed by Krauss, Nasri, and Trodden (KNT) [47] extends the SM with new scalars and a right handed neutrino playing the role of the dark matter. More recently a variation of the KNT model was introduced and incorporates a fermion triplet to generate neutrino masses at the three-loop level [48]. However, unlike our framework, the new fields are not charged under colour and quarks do not play an active role in the generation of neutrino masses. Within our framework, the three-loop diagram is due to exchanges of both ψ and χ fields. The mechanism is depicted in Figure 5. However within this framework, the loop is closed through an effective $\psi\psi\chi_1\chi_1$ vertex parametrized by an effective coupling, ρ . This vertex is both hypercharge and weak isospin changing. One way of generating this vertex is by introducing a coloured electroweak-triplet scalar, ω

$$\omega = \begin{pmatrix} \omega_2/\sqrt{2} & \omega_1 \\ \omega_3 & -\omega_2/\sqrt{2} \end{pmatrix}, \quad (16)$$

with no tree-level coupling to fermions. The field ω transforms as a $(\mathbf{3}, \mathbf{3}, \mathbf{2}/\mathbf{3})$ under the SM gauge group and it is even under Z_2 . We add to the scalar potential, Equation (3), the terms involving ω

$$V(H, \psi, \chi, \omega) = m_\omega^2 \omega^\dagger \omega + \lambda_\omega (\text{Tr} \omega^\dagger \omega)^2 + \kappa_4 H^\dagger H \text{Tr} \omega^\dagger \omega + \kappa_5 H^\dagger \omega^\dagger \omega H \\ + \rho_2 (\text{Tr} \omega^\dagger \omega) \psi^\dagger \psi + \rho_3 \text{Tr} (\omega^\dagger \psi \omega^\dagger \psi) + \alpha \text{Tr} H^T i \sigma_2 \chi \omega^\dagger H + \tilde{V}(\chi, \omega) + \text{h.c.}, \quad (17)$$

where $\tilde{V}(\chi, \omega)$ parametrizes all renormalizable quartic couplings between χ and ω . Electroweak symmetry breaking leads to $\chi - \omega$ mixing given approximately by $\theta_{\chi-\omega} \sim \alpha v^2 / (m_\omega^2 - m_\chi^2)$ with $v = \langle H \rangle = 174$ GeV. Barring accidental degeneracy between χ and ω this mixing is expected to be small. Thus, the ρ_3 coupling in the scalar potential yields a four scalar coupling involving $\psi\psi\omega_2^\dagger\omega_2^\dagger$ and an effective vertex between $\psi\psi\chi_1\chi_1$ arises and it is given by

$$\rho = \rho_3 \cdot \theta_{\chi-\omega}. \quad (18)$$

Since ω has no couplings to fermions it has less interesting phenomenology than χ although its mass is of order m_χ . Furthermore, the effective ρ vertex may also arise from higher scale physics.

Armed with the above we obtain finite contributions to the ℓ, ℓ' elements of the active neutrino mass matrix M^ν . These can be written as

$$(M^\nu)_{\ell\ell'} = \sum_{i,j} K^{ij} \lambda_\ell^i \lambda_{\ell'}^j, \quad (19)$$

where $i, j = u, c, t$. The K^{ij} factor controls the scale of neutrino masses and it is given by

$$K^{ij} = \frac{y_\psi^i y_\psi^j \rho}{(16\pi^2)^3} \frac{m_i m_j M_{N_R}^3}{(m_\chi^2 - m_i^2)(m_\chi^2 - m_j^2)} I(m_\psi^2, m_\chi^2, m_i^2, m_j^2),$$

$$I(m_\psi^2, m_\chi^2, m_i^2, m_j^2) = \int_0^\infty du \frac{u}{u+1} f(u, m_i^2, m_\psi^2, m_\chi^2) f(u, m_j^2, m_\psi^2, m_\chi^2)$$

$$f(u, m^2, m_\psi^2, m_\chi^2) = \int_0^1 dx \ln \left(\frac{m_\chi^2(1-x) + m_\psi^2 x + M_{N_R}^2 u x(1-x)}{m^2(1-x) + m_\psi^2 x + M_{N_R}^2 u x(1-x)} \right). \quad (20)$$

This reveals the workings of a generalized seesaw mechanism. The seesaw scale here is m_χ . In the limit $M_{N_R} \rightarrow 0$ there is a conserved lepton number and therefore the active neutrinos will remain massless. Dimensional arguments give the other mass ratios in Equation(20) as the integrals are dimensionless.

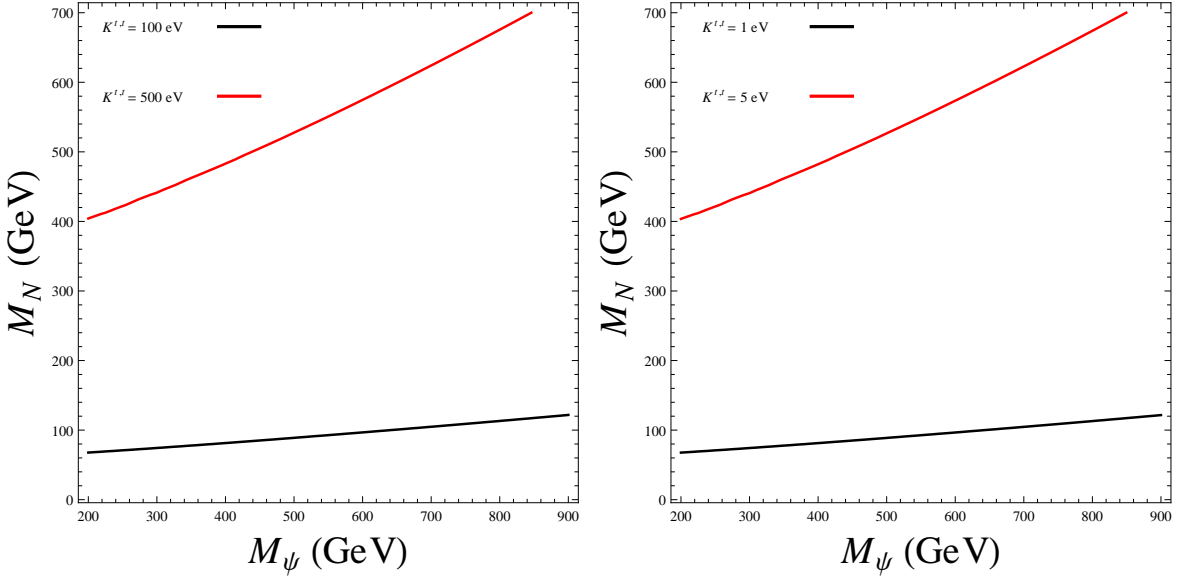


FIG. 6. $K^{t,t}$ factor in the $M_{N_R} - m_\psi$ plane. (a)Left: $y_\psi^t = 1$ and $y_\psi^{c/u} \approx 0$. The red and black lines correspond to $K^{t,t} = 500, 100$ eV respectively. (b)Right: $y_\psi^t \approx 0$ and $y_\psi^{c/u} = 1$. The red and black lines correspond to $K^{t,t} = 5, 1$ eV.

Numerically it is easy to see that the important contributions come from the t - and c -quarks without fine tuning of the Yukawa couplings. Moreover, if only one generation of quarks contributes, such as the t -quark, then it will give rise to two massless active neutrinos which is ruled out by neutrino oscillation data. Thus, at least two quark generations must come into play. This will result in one massless neutrino, which is consistent with current data. If all three neutrinos were to be found to have non zero masses, then the u -quark must also be included. We note that another solution for light neutrino masses would be to add one or two more N_R but we don't pursue this alternative here.

In this work we update the results presented in [33] in various interesting regions of parameter space. We choose to vary only the mass of the coloured electroweak-singlet scalar and the Majorana neutrino, N_R . We use a coloured electroweak-triplet scalar with mass $m_\chi = 1$ TeV and a scalar potential coupling $\rho = 0.1$ as benchmark points. In addition, we keep the leading contribution to the masses of the active neutrinos coming from the t -quark. In Figure 6(a) we present the $K^{t,t}$ factor in the $M_{N_R} - m_\psi$ plane for $y_\psi^t = 1$ and $y_\psi^{c/u} \approx 0$. The red and black lines correspond to $K^{t,t} = 500, 100$ eV respectively. We emphasize that values of $K^{t,t}$ below 100 eV are possible for small Majorana masses and large values of m_ψ . Figure 6(b) corresponds to $y_\psi^t \approx 0$ and $y_\psi^{c/u} = 1$. The red and black lines correspond to $K^{t,t} = 5, 1$ eV. In this region of parameter space, a $K^{t,t}$ factor in the meV range is possible for small values of M_{N_R} and large values of m_ψ .

V. CONSTRAINTS

In the following subsections we discuss the main constraints on our model. In particular, we look at the regions of parameter space excluded by lepton flavour violating decays, rare decays of the top quark and the existence of new modes for Higgs decay and production. Furthermore, we look at the latest collider searches for dark matter by the CMS collaboration in the jets + MET and monojet channels.

A. $\mu \rightarrow e\gamma$ and rare b decays

Although the dark matter calculation is not sensitive to the masses of the coloured electroweak-triplet states, they can give rise to lepton flavour violating decays such as $\mu \rightarrow e\gamma$ as well as a contribution to the muon anomalous magnetic moment, a_μ . Both contributions come in at the 1-loop level. Interestingly, the singlet state ψ does not contribute to these processes at this level. The Feynman diagrams for the $\mu \rightarrow e\gamma$ decay process are depicted in Figure 7.

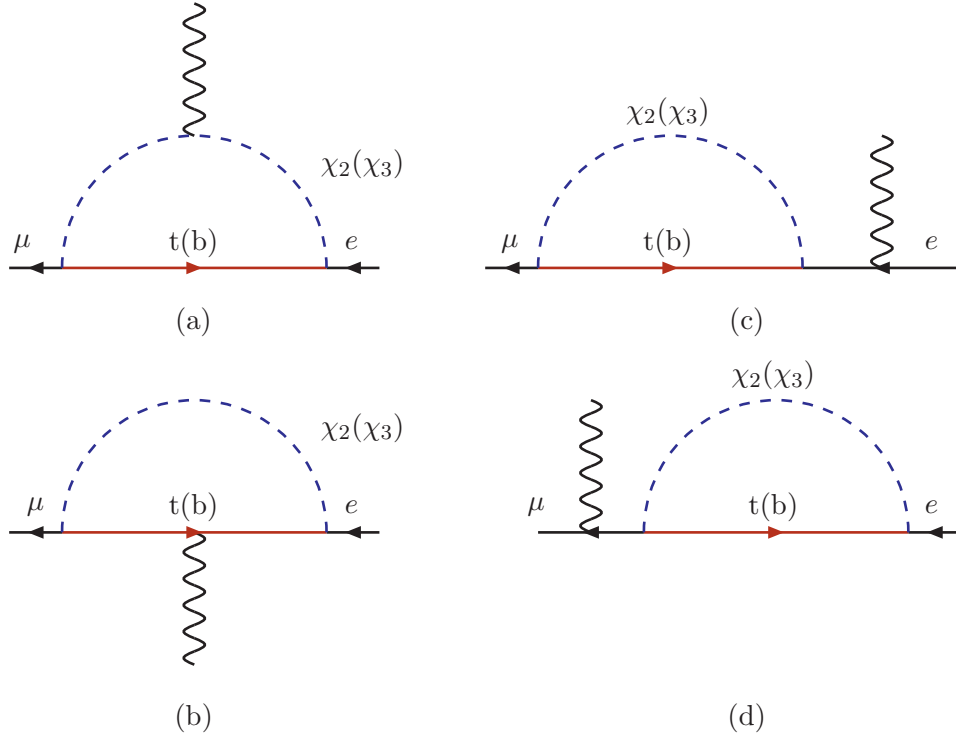


FIG. 7. 1-loop diagrams for $\mu(p) \rightarrow e(p') + \gamma(q)$ decays. The arrows indicate fermion charge flow. Main contribution comes from (a) and (b) whereas (c) and (d) are needed to enforce gauge invariance. Similar diagrams from the second generation quarks are not displayed

The effective Lagrangian for the decay can be written as

$$\mathcal{L} = A \bar{e} i \sigma^{\mu\nu} (1 + \gamma^5) \mu F_{\mu\nu}. \quad (21)$$

The decay width is given by

$$\Gamma(\mu \rightarrow e\gamma) = \frac{|A|^2 m_\mu^3}{16\pi}, \quad (22)$$

where a standard calculation yields the following expression for A

$$A = \frac{em_\mu}{64\pi^2 m_\chi^2} \sum_{i=t,c,u} \frac{\lambda_\mu^i \lambda_e^i}{(1-a_i)^3} \left[3 - 10a_i - 5a_i^2 + \frac{2a_i - 16a_i^2}{1-a_i} \ln a_i \right] \quad (23)$$

$$\xrightarrow{a_i \rightarrow 0} \frac{3e}{64\pi^2} \left(\frac{m_\mu}{m_\chi^2} \right) \sum_{i=t,c,u} \lambda_\mu^i \lambda_e^i.$$

In the above equation we have assumed a common mass, m_χ , for both χ_2 and χ_3 and defined $a_i = \frac{m_i^2}{M_\chi^2}$. We have also neglected terms of $O((m_{t(b)}/M)^2)$. Therefore, the branching fraction is given by

$$Br(\mu \rightarrow e\gamma) = 1.8 \left(\frac{\text{TeV}}{m_\chi} \right)^4 \times 10^{-6} |\lambda_\mu^t \lambda_e^t + \lambda_\mu^c \lambda_e^c + \lambda_\mu^u \lambda_e^u|^2. \quad (24)$$

Since in our framework $K^{t,t} \gg K^{c,c}, K^{u,u}$, our calculations are not sensitive to the value of $\lambda_\mu^c \lambda_e^c$ which appears in Equation (19). Furthermore, we can set $\lambda_l^u \sim 0$ in order to suppress rare kaon decays. In order to analyze the constraints arising from this rare decay, we maximize the contribution from new physics by working in the limit where $\lambda_\mu^c \lambda_e^c \sim \lambda_\mu^t \lambda_e^t$ and set $m_\chi = 1$ TeV. In order to extract an upper bound on the value of $\lambda_\mu^t \lambda_e^t$ we follow the analysis in [33] where we made use of the latest best fit value for $M_{e\mu}^\nu$ [49] assuming a normal hierarchy with $m_1 \rightarrow 0$, and the current experimental bound on $Br(\mu \rightarrow e\gamma) \leq 2.4 \times 10^{-12}$ [50]. With this in mind we can rewrite Equation (24) using Equation (19):

$$Br(\mu \rightarrow e\gamma) = 7.2 \times 10^{-6} \left(\frac{M_{e\mu}^\nu}{K^{t,t}} \right)^2. \quad (25)$$

Similar diagrams to those contributing to $\mu \rightarrow e\gamma$ contribute to the decay $b \rightarrow s\gamma$. This decay has a SM contribution which is the same as the amplitude arising from our new physics. The data [51] is consistent with the SM expectation and we obtain the following limit:

$$\sum_l |\lambda_l^b \lambda_l^s| < 0.104 \left(\frac{m_\chi}{\text{TeV}} \right), \quad (26)$$

where we have set $\lambda_l^{b,s} = \lambda_l^{t,c}$. Furthermore, recent results from the LHCb and CMS collaborations have found a branching ratio for the decay $B_s^0 \rightarrow \mu^+ \mu^-$ of $2.9_{-1.0}^{+1.1} \times 10^{-9}$ [52] and $3.0_{-0.9}^{+1.0} \times 10^{-9}$ [53] consistent with the SM expectation of $3.2 \pm 0.2 \times 10^{-9}$. Within our framework, this decay can be induced through the exchange of the coloured electroweak-triplet, χ_3 , and it sets the following bound on the product $\lambda_\mu^b \lambda_\mu^s$:

$$\lambda_\mu^b \lambda_\mu^s < 3.4 \times 10^{-3} \left(\frac{m_\chi}{\text{TeV}} \right). \quad (27)$$

In [33] we found that values of λ_l^i below 0.1, required for sub-eV neutrino masses, are consistent with constraints from rare b decays.

B. Rare top decays

Within our framework both types of Yukawa couplings, λ_l^i 's and y_ψ^i 's, are involved in the mechanism that leads to neutrino masses. In Section V A we saw that the decay $\mu \rightarrow e\gamma$ can directly constrain $\lambda_\mu^i \lambda_e^i$, in particular $\lambda_\mu^t \lambda_e^t$ which is inversely proportional to $(y_\psi^t)^2$. However, the following rare decays of the top, $t \rightarrow g c$, $t \rightarrow \gamma c$ and $t \rightarrow Z c$ will be sensitive to y_ψ^c . The dominant decay mode is $t \rightarrow g c$ since this has a large colour charge. This mode can be probed at the LHC through single top production via gluon and c -quark fusion. The SM contributions are negligible and this mode can provide a very sensitive probe for new physics. In particular, the gluon plus c mode is useful for probing new colour degrees of freedom such as the ψ and χ scalars. In our framework, due to the special role that ψ plays in the annihilation of the dark matter candidate, N_R , we consider coloured electroweak-singlet states that are much lighter than the coloured electroweak-triplet scalars. The effective Lagrangian for this decay is given by

$$\mathcal{L} = A_g^a \bar{c} i \sigma^{\mu\nu} P_R t G_{\mu\nu}^a, \quad (28)$$

where $G_{\mu\nu}$ is the gluon field tensor. The dipole form factor A_g can be calculated from diagrams similar to those that contribute to $\mu \rightarrow e\gamma$ and it is given by:

$$A_g^a = i \frac{y_\psi^t y_\psi^{*c} g_s}{16\pi^2} \frac{m_t}{m_\psi^2} T^a I(x_N, x_t), \quad (29)$$

where g_s is the QCD coupling, T^a is a colour $SU(3)$ generator and $x_i = \frac{m_i^2}{M_\psi^2}$ for a particle of mass m_i . The integral I is given explicitly by

$$I(a, b) = \int_0^1 dx \int_0^{1-x} dy \frac{1 - x - y}{x + y + a(1 - x - y) - bx(1 - x - y)}, \quad (30)$$

where the c -quark mass can be neglected at these energies. For the case of relatively light Majorana neutrinos, i.e. $x_{NR} \ll 1$, the integral can be expressed in analytic form

$$I(0, b) = \frac{1}{6b} \left[-6 \ln(1-b)(1-b+b \ln b) + b(-6 + \pi^2 - 3b + 3 \ln^2 b) + 6b \text{Li}_2(1-b^{-1}) \right]. \quad (31)$$

A recent ATLAS analysis searching for flavour changing neutral currents in single top quark production with an integrated luminosity of 2.05 fb^{-1} at a centre of mass energy of $\sqrt{s} = 7 \text{ GeV}$ [54] can be used to place an upper bound on the parameters of our model. This bound is given by

$$\frac{y_\psi^t y_\psi^c m_t}{32\pi^2 m_\psi^2} I(x_N, x_t) < 1.6 \times 10^{-2} \text{TeV}^{-1}. \quad (32)$$

C. $D^0 - \bar{D}^0$ Oscillations

Within our framework, both u - and c -quarks can couple to the coloured electroweak-singlet and the Majorana neutrino for non-zero values of $y_\psi^{u,c}$. Couplings of this type can yield sizeable contributions to the mass difference, ΔM_D , in $D^0 - \bar{D}^0$ mixing. Meson-antimeson mixing is sensitive to heavy degrees of freedom and as such can significantly constrain the validity of our model. The relevant quantities in $D^0 - \bar{D}^0$ mixing are the mass difference, ΔM_D , and the width difference, $\Delta \Gamma_D$, that can be parametrized by the following equations:

$$x_D = \frac{\Delta M_D}{\Gamma_D} \\ y_D = \frac{\Delta \Gamma_D}{2\Gamma_D}, \quad (33)$$

where Γ_D is the average width of the two neutral D meson mass eigenstates. A current fit to these two variables by the HFAG collaboration gives $x_D = 0.43_{-0.16}^{+0.15}\%$, $y_D = 0.65 \pm 0.08\%$ [51].

Given the uncertainty in the SM long distance contribution to ΔM_D , we assume that ΔM_D is driven primarily by contributions from this model. This gives us a tighter constraint on our model than assuming that the SM long distance contribution is comparable to the size of ΔM_D . Following the analysis of the implications of $D^0 - \bar{D}^0$ mixing for new physics [55], our contribution to x_D is given by

$$x_D = \frac{1}{M_D \Gamma_D} \text{Re} \left[2 \left\langle \bar{D}^0 | H_{NP}^{|\Delta C|=2} | D^0 \right\rangle \right], \quad (34)$$

where we can use the operator product expansion and the renormalization group to define

$$\left\langle \bar{D}^0 | H_{NP}^{|\Delta C|=2} | D^0 \right\rangle = G \sum_{i=1} C_i(\mu) \left\langle \bar{D}^0 | Q_i | D^0 \right\rangle(\mu). \quad (35)$$

In the above equation G is a coefficient with inverse squared mass dimension, C_i are Wilson coefficients, and $\left\langle \bar{D}^0 | Q_i | D^0 \right\rangle$ are effective operators. In our framework, the Lagrangian in Equation 2 yields the following operator at the scale where the heavy degrees of freedom are integrated out,

$$Q_6 = (\bar{u}_R \gamma_\mu c_R) (\bar{u}_R \gamma^\mu c_R). \quad (36)$$

To take into account the operator mixing between Q_6 and the other 7 operators listed in [55] that arise from the renormalization group running between the scale of new physics and the charm mass m_c , we solve the renormalization group equations obeyed by the Wilson coefficients. With this in mind, we obtain a contribution to the mass difference given by

$$\Delta M_D = \frac{(y_\psi^u y_\psi^c)^2 f_D M_D}{64\pi^2 m_\psi} \frac{2}{3} B_D \beta(m_c, m_\psi) |\text{L}(\eta)|, \quad (37)$$

where we have used the values $f_D = 212 \times 10^{-3} \text{ GeV}$ and $B_D = 0.82$ for the D -meson decay constant and Bag constant respectively. Furthermore, we have used an average D -meson mass of $M_D = 1.865 \text{ GeV}$, a renormalization group factor $\beta(m_c, m_\psi)$ given by

$$\beta(m_c, m_\psi) = \left(\frac{\alpha_s(m_\psi)}{\alpha_s(m_t)} \right)^{2/7} \left(\frac{\alpha_s(m_t)}{\alpha_s(m_b)} \right)^{6/23} \left(\frac{\alpha_s(m_b)}{\alpha_s(m_c)} \right)^{6/25}, \quad (38)$$

and the loop integral factor $L(\eta)$ given by

$$L(\eta) = \frac{\eta}{(1-\eta)^2} \left[1 + \frac{1}{(1-\eta)} \log \eta \right], \quad (39)$$

with $\eta = \frac{M_{NB}^2}{m_\psi^2}$.

D. Higgs production and decay

The discovery of a 125 GeV SM-like Higgs boson at the LHC [56, 57] has placed strong bounds on models that modify how the Higgs is produced and how it decays. In our model, the new coloured scalar degrees of freedom contribute, at one loop, to SM Higgs production through gluon fusion, and Higgs decays into photons. Since in our framework the coloured electroweak-singlet, ψ , may lie below the TeV scale, the relevant operator contributing to Higgs production and decay after electroweak symmetry breaking (EWSB) is given by

$$\kappa_3 H^\dagger H \psi^\dagger \psi \rightarrow \kappa v H \psi^\dagger \psi, \quad (40)$$

where $v = \langle H \rangle = 174$ GeV. The LHC is now able to restrict the couplings of these new coloured scalars to the SM-like Higgs boson. An analysis in [58] studied the contributions to the Higgs decay width into photons that arise from coloured scalars. Using standard notations, the Higgs diphoton decay width, including only new spin-0 contributions, is given by

$$\Gamma_{\gamma\gamma} \equiv \Gamma(H \rightarrow \gamma\gamma) = \frac{G_\mu \alpha^2 M_H^3}{128 \sqrt{2} \pi^3} \left| F_1(\tau_W) + \frac{4}{3} F_{1/2}(\tau_t) + d(r_\psi) Q_\psi^2 \frac{\kappa_3}{g_w} \frac{M_W^2}{m_\psi^2} F_0(\tau_\psi) \right|^2, \quad (41)$$

where $Q_\psi = 2/3$ and $d(r_\psi) = 3$ are the charge and dimension of the representation of the coloured electroweak-singlet. The functions F_1 , $F_{1/2}$ and F_0 are given by

$$\begin{aligned} F_0(\tau) &= -[\tau - f(\tau)]\tau^{-2} \\ F_{1/2}(\tau) &= 2[\tau + (\tau - 1)f(\tau)]\tau^{-2} \\ F_1(\tau) &= -[2\tau^2 + 3\tau + 3(2\tau - 1)f(\tau)]\tau^{-2}, \end{aligned} \quad (42)$$

where

$$f(\tau) = \begin{cases} \arcsin^2 \sqrt{\tau} & \tau \leq 1 \\ -\frac{1}{4} \left[\log \frac{1+\sqrt{1-\tau^{-1}}}{1-\sqrt{1-\tau^{-1}}} - i\pi \right]^2 & \tau > 1 \end{cases} \quad (43)$$

and $\tau_i = M_H^2/4M_i^2$.

The analysis on additional contributions to the production of a SM-like Higgs boson through gluon fusion was carried out in a similar fashion to the diphoton Higgs decay [58]. In particular, the parton level cross section for $gg \rightarrow H$ is given by

$$\sigma_{gg} \equiv \hat{\sigma}(gg \rightarrow H) = \sigma_0 M_H^2 \delta(\hat{s} - M_H^2), \quad (44)$$

where

$$\sigma_0 = \frac{G_\mu \alpha_s^2}{128 \sqrt{2} \pi} \left| \frac{1}{2} F_{1/2}(\tau_t) + C(r_\psi) \frac{\kappa_3}{g_w} \frac{M_W^2}{m_\psi^2} F_0(\tau_\psi) \right|^2, \quad (45)$$

and $C(r_\psi) = 1/2$ is the index of the representation of ψ .

Recent results from the LHC suggest a slight enhancement on the diphoton Higgs decay channel. In particular, the ATLAS collaboration measured a $\sigma/\sigma_{SM} = 1.65 \pm 0.24$ (stat) $^{+0.25}_{-0.18}$ (syst) [59]. The CMS result of 1.11 ± 0.31 [60] appears to be consistent with the SM. We use these two results and Equation 45 to place an upper bound on the value of κ_3 which can be written as:

$$\kappa_3 \lesssim 5.31 \quad (46)$$

for $m_\psi = 200$ GeV and $\kappa_3 > 0$.

E. Collider Constraints

One important feature of our model is that it contains new coloured degrees of freedom which can be produced in hadron colliders such as the LHC. In particular, the coloured electroweak-singlet, ψ , can be pair produced and it can later decay to top and/or up quarks and a large component of missing transverse energy carried away by N_R . Additionally, it can be singly produced in association with N_R leading to a monojet signal. A monojet signal is also viable through pair production of Majorana neutrinos after taking into account initial and final state radiation as well as jets emitted from an intermediate coloured electroweak-singlet, ψ . In what follows we discuss the different searches carried out by the CMS collaboration used to constrain the parameter space considered in this work.

1. Limits from jets+MET

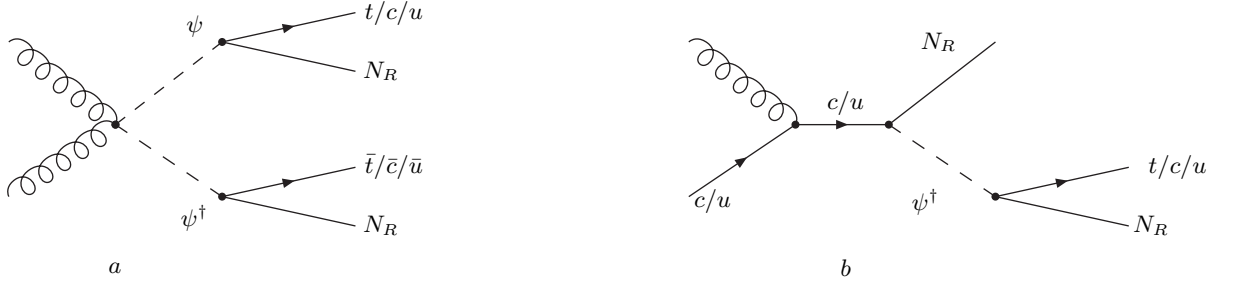


FIG. 8. Leading order Feynman diagrams the lead to jets plus MET final states at the LHC. The diagram on the left will also lead to a $t\bar{t}$ plus MET signature and can be constrained by searches for scalar top pair production [65].

In this section we look at the possibility of setting limits to our model by considering searches for jets + MET at hadron colliders. We focus on a search for multijets and missing momentum with 19.5 fb^{-1} of data at $\sqrt{s} = 8 \text{ TeV}$ by the CMS collaboration [19]. In our framework there are various topologies that lead to a multijet plus missing momentum final state, these are depicted in Figures 8 and 9. For small couplings, $y_\psi^{c,u}$, the dominant channel is depicted in 8(a). In fact, this diagram resembles pair production of scalar quarks (squarks) in supersymmetry with a final state containing between two and six jets for arbitrary choices of the couplings $y_\psi^{t,c,u}$. For large $y_\psi^{c,u}$ couplings, the production cross section is enhanced via the diagram depicted in Figure 9(a) since a Majorana fermion mediates the reaction. This enhancement is more pronounced for large M_{N_R} .

The CMS collaboration [19] implements a selection criteria on the number of jets, N_{jets} , with a transverse momentum of $p_T > 50 \text{ GeV}$ and a pseudorapidity of $|\eta| < 2.5$. Furthermore, each event is required to have MET above 150 GeV. They consider signal regions where $N_{jets} = 3 - 5, 6 - 7$ and ≥ 8 . To estimate the current bounds, we simulate the leading order cross section for the processes depicted in Figures 8 and 9 using MadGraph 5 [62] for masses of the right-handed Majorana neutrino, N_R , and the coloured electroweak-singlet, m_ψ , for different regions of the couplings $y_\psi^{t,c,u}$. The parton showering and hadronization is carried out with PYTHIA [63] and employ the Delphes 3 detector simulator package [64] to calculate our acceptances. Since our signal is inclusive, we carry out the matching between the hard and low energy scales using the MLM matching scheme where parton events generated by MadGraph are matched to jets from the perturbative shower to avoid double counting.

The sensitivity of the CMS search to our model for $y_\psi^t \rightarrow 1$ and small $y_\psi^{c,u}$ decreases dramatically since now the pair produced coloured singlet scalars will decay predominantly to t -quarks plus MET. In this particular case, the signal region most sensitive to our model is one where $N_{jets} = 6 - 7$; however since the analysis does not implement a t -quark reconstruction algorithm, the regions with the highest energy jets are those where ψ has a large mass and thus a smaller production cross section. The signal regions where $N_{jets} = 3 - 5$ lead to a large number of signal events but not enough to overcome the large systematic uncertainties in the calculated background, mainly the contribution from QCD. The sensitivity of the CMS search to our model in the large $y_\psi^{c,u}$ limit is strongest for large Majorana masses and away from the degenerate region $m_\psi \approx M_{N_R}$, where high p_T jets from the decay of the coloured electroweak-singlet are more prominent.

In our analysis we implement eight signal regions from a combination of the number of high energy jets, N_{jets} , the visible hadronic activity, $H_T = \sum_{N_{jets}} |p_T|$, and the momentum imbalance $\cancel{H}_T = |-\sum_{jets} \vec{p}_T|$, and calculate a 95% confidence level exclusion limit in the $M_{N_R} - m_\psi$ plane for three sets of fixed couplings $(y_\psi^t, y_\psi^c, y_\psi^u) =$

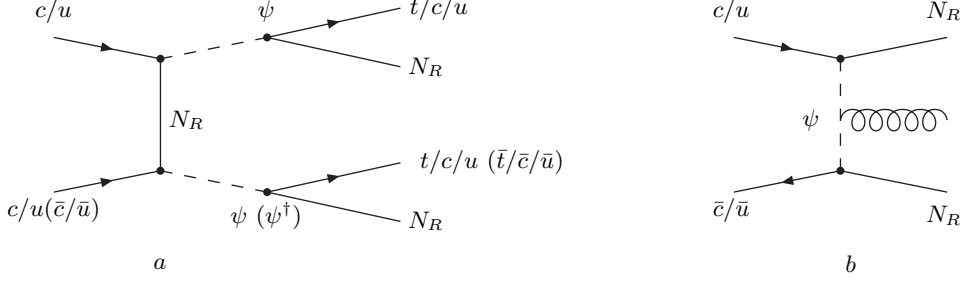


FIG. 9. Leading order Feynman diagrams that lead to jets plus MET final states at the LHC and that enhance the production rate at large $y_{\psi}^{t,c,u}$. The diagram on the right contributes to same-sign top (anti-top) production at the LHC.

(1, 0.1, 0.1), (1, 0.01, 0.5), (0.4, 0.01, 1). These benchmark scenarios are motivated by the constraints discussed in the previous subsections, in particular, a suppression of $D^0 - \bar{D}^0$ oscillations, a small contribution to the decay of $\mu \rightarrow e\gamma$ and natural neutrino masses.

2. Limits from monojets

Here we discuss how we can set limits to our model by considering searches for monojets at hadron colliders. We focus on a search for monojet events with 19.5 fb^{-1} of data at $\sqrt{s} = 8 \text{ TeV}$ by the CMS collaboration [18]. Within our framework the topologies that may lead to a final state with one high energy jet and missing momentum are depicted in Figures 8(b) and 9(b). For small values of the coupling $y_{\psi}^{c,u}$, the topology in Figure 8(b) dominates. This enhancement is more prominent when the coloured electroweak-singlet is produced on-shell. As the value of the $y_{\psi}^{c,u}$ coupling increases the diagram depicted in Figure 9(b) will enhance the cross section when a jet is emitted from the intermediate ψ state. The CMS analysis requires a jet with $p_T > 110 \text{ GeV}$ and a second jet with a $p_T > 30 \text{ GeV}$. The two jets require a separation of $\Delta\phi < 2.5$ to suppress QCD dijet events. We simulate the leading order cross section for $p p \rightarrow N_R N_R j$. In our analysis we consider four signal regions in missing transverse energy: MET = 250, 300, 350, 550 GeV, and calculate a 95% confidence level exclusion limit in the $M_{N_R} - m_{\psi}$ plane for three representative sets of fixed couplings $(y_{\psi}^t, y_{\psi}^c, y_{\psi}^u) = (1, 0.1, 0.1), (1, 0.01, 0.5), (0.4, 0.01, 1)$.

3. Limits from top squark pair production and same-sign tops

Additionally, one may place limits from searches for top squark pair production at hadron colliders. In this section we focus on a search for top squark pair production in the single lepton final state with 19.5 fb^{-1} of data at $\sqrt{s} = 8 \text{ TeV}$ by the CMS collaboration [65]. Within our framework, the topologies that lead to a $t\bar{t}$ and MET final state are depicted in Figure 8(a) and Figure 9(a) for large $y_{\psi}^{c,u}$. To estimate the current bounds we simulate the leading order cross section for $p p \rightarrow \psi\psi^\dagger$ using MadGraph [62] for masses of the right-handed Majorana neutrino, N_R , and the coloured electroweak-singlet, m_{ψ} , for different regions of the couplings $y_{\psi}^{c,t}$. Furthermore, we use Madgraph to decay the coloured electroweak-singlet to $N_R t$. We use PYTHIA [63] to decay the top quark and for parton showering and hadronization.

The sensitivity of the CMS search to our model is strongest for $y_{\psi}^t \rightarrow 1$ and $y_{\psi}^{c,u} \rightarrow 0$ since in this region of parameter space $BR(\psi \rightarrow N_R t) \approx 1$. In our analysis we consider three signal regions in missing transverse energy: MET = 150, 200, 300 GeV. It is important to note that the topologies contributing to this analysis also lead to a final state with jets plus MET. However, the former has the advantage that top tagging is implemented. This is done by demanding that three jets in the event originate from a top quark. This allows us to remove a larger amount of background without demanding jets with large p_T . In order to derive limits on the parameter space of the model, we calculate a 95% confidence level exclusion limit in the $M_{N_R} - m_{\psi}$ plane for three sets of fixed couplings $(y_{\psi}^t, y_{\psi}^c, y_{\psi}^u) = (1, 0.1, 0.1), (1, 0.01, 0.5), (0.4, 0.01, 1)$.

In addition, the diagram depicted in Figure 9(a) yields a same-sign top final state. Same-sign top production yields a signal with two same-sign leptons which has a low background rate in the SM. Within our framework this final state is mediated by a Majorana fermion and thus is enhanced for large M_{N_R} . Since $m_{\psi} > M_{N_R}$ within our framework, one would equally need large ψ masses with smaller production rates. Furthermore a large coupling, y_{ψ}^u , is required, but

this has the effect of suppressing the decay rate $\psi \rightarrow t N_R$. Therefore, we expect current searches for same-sign top quarks to have little constraining power on our parameter space. We focus on a search for new physics in events with same-sign dileptons with 19.5 fb^{-1} of data at $\sqrt{s} = 8 \text{ TeV}$ by the CMS collaboration [66]. We consider four signal regions specified by the number of b -jets and whether there is a discriminant on the sign of the dilepton system.

VI. RESULTS

In this section we present the results from a scan on the masses for the coloured electroweak-singlet scalar and the mass of the Majorana neutrino, N_R , for three sets of fixed couplings $(y_\psi^t, y_\psi^c, y_\psi^u) = (1, 0.1, 0.1), (1, 0.01, 0.5), (0.4, 0.01, 1)$. In order to show the available parameter space consistent with the present dark matter abundance and all of the constraints discussed in the previous section, we present our results in the $m_\psi - M_{N_R}$ plane.

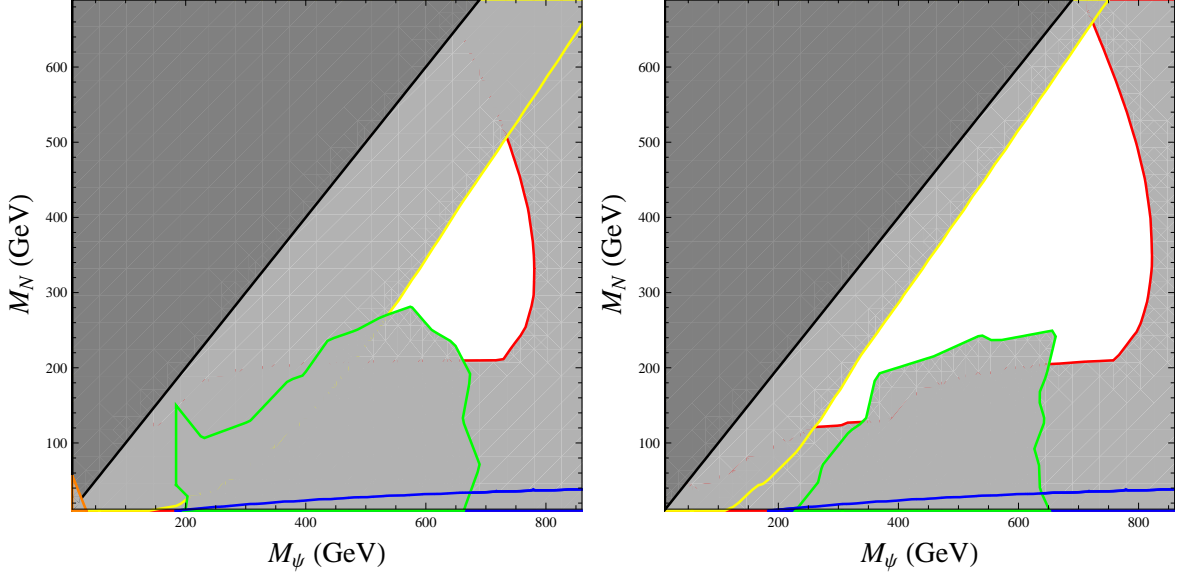


FIG. 10. Allowed region of parameter space consistent with the density of dark matter as measured by Planck [6] (red solid line) after taking into account all constraints discussed in Section V for $y_\psi^t = 1$ and $y_\psi^{c,u} = 0.1$ on the left and $y_\psi^t = 1$ and $y_\psi^{c,u} = 0.01, 0.5$ on the right. The region in white is allowed but our dark matter annihilates too efficiently in the early universe.

In Figure 10(a) the region consistent with the density of dark matter as measured by Planck [6] is depicted by a red solid line for $y_\psi^t = 1$ and $y_\psi^{c,u} = 0.1$. The dark grey region is excluded since we have assumed that $m_\psi > M_{N_R}$ in order for N_R to be the lightest stable particle under the dark parity. The region below the green solid line is excluded by searches for pair produced top squarks at the LHC. This is consistent with what we discussed in Section V E 3 where in the limit $y_\psi^t \rightarrow 1$ and $y_\psi^{c,u} \rightarrow 0$ the branching ratio $BR(\psi \rightarrow N_R t) \approx 1$, thus the coloured electroweak-singlet resembles a top squark that decays to a top quark and a neutralino as in supersymmetric extensions of the Standard Model. The region below the blue solid line is excluded by the lepton flavour violating decay, $\mu \rightarrow e \gamma$. The lack of constraining power is due to the fact that the branching fraction for this decay is inversely proportional to $K^{t,t}$, which is proportional to $(y_\psi^t)^2$. The region above the solid yellow line is excluded by $D^0 - \bar{D}^0$ oscillations and it is relaxed with small y_ψ^c and/or y_ψ^u , as can be seen in Equation (37). Constraints arising from new SM-like Higgs production and decay modes did not exclude additional parameter space for coloured electroweak-singlet masses below 1 TeV and values of the scalar potential coupling appearing in Equation (3) $\kappa_3 \leq 1$. The remaining light grey region is excluded since it leads to an overabundance of the Majorana neutrino. Similarly, in Figure 10(b) the region consistent with the density of dark matter is depicted by a red solid line for $y_\psi^t = 1$ and $y_\psi^{c,u} = 0.01, 0.5$. The region excluded by the decay $\mu \rightarrow e \gamma$ is the same as the former parameter set since $K^{t,t} \gg K^{c,c}, K^{u,u}$. In Figure 11 we show in red the regions consistent with the dark matter relic abundance for $y_\psi^t = 0.4$ and $y_\psi^{c,u} = 0.01, 1$. The region below the green solid line is excluded by the CMS stop pair production search. This region is smaller since $Br(\psi \rightarrow N_R t)$ is suppressed compared to the regions where $y_\psi^t = 1$. The region below the orange solid line is excluded by the CMS jets + MET search. The region below the solid purple line is excluded by the CMS monojet search. This exclusion dominates since a coupling of y_ψ^u yields a large cross section for the diagrams depicted in Figures 8(b) and 9(b). Our

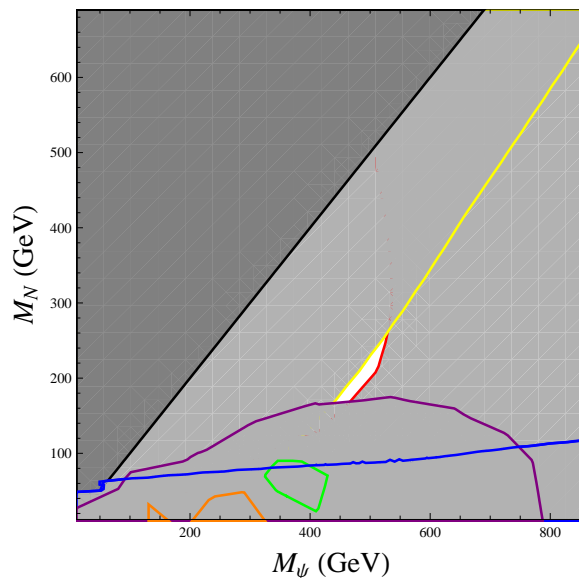


FIG. 11. Allowed region of parameter space consistent with the density of dark matter as measured by Planck [6] (red solid line) after taking into account all constraints discussed in Section V for $y_\psi^t = 0.4$ and $y_\psi^{c,u} = 0.01, 1$. The region in white is allowed but the dark matter annihilates too efficiently in the early universe.

results show that the most constraining scenario is when $y_\psi^t \rightarrow 0$, since in this case, contributions to flavour violating decays are very large. In the analysis that follows we chose to work in the limit where $y_\psi^c \rightarrow 0$ in exchange for a potentially large monotop production rate which gets enhanced with an up -quark in the initial state.

Thus, we see that in all scenarios considered in this study, coloured electroweak-singlets with masses between 400 – 600 GeV and Majorana neutrino masses between 150 – 600 GeV can yield the correct dark matter abundance while being consistent with all current experimental searches. Furthermore, we see that a light Majorana neutrino with mass below 150 GeV is possible if we let $y_\psi^c \rightarrow 0$, relaxing the bounds arising from $D^0 - \bar{D}^0$ oscillations. However, this is not the only recipe for a large monotop signature (large amount of \cancel{E}_T) within our framework since for this region of parameter space the colored electroweak-singlet is also relatively light. In addition, a large monotop production rate requires a large y_ψ^u region that is ruled out by direct searches for dark matter in the light m_ψ scenario, Figures 4(a) and 4(b). In the following section we analyze the prospects of generating a monotop signal that could be probed with the current data set at the LHC and in the future 14 TeV run.

VII. MONOTOP PRODUCTION

In this section we discuss the monotop signal within our framework. The CDF collaboration reported on a search for dark matter using 7.7 fb^{-1} of integrated luminosity and $p\bar{p}$ collisions at $\sqrt{s} = 1.96 \text{ TeV}$ [67]. Within the framework of effective field theories, they were able to place an upper bound on the production cross section of a dark matter particle in association with a single top quark. Their reach extends to dark matter masses below $\sim 150 \text{ GeV}$ and we found that implementing this analysis does not constrain our model beyond the constraints discussed in Section V.

We simulate our signal with an additional jet, that is, contributions to the rate arise from the diagram depicted in Figures 12 as well as Figures 8(a) and 9(a) where one coloured electroweak-singlet decays to a top quark while the other to a light jet. We implement a search strategy at the LHC in the hadronic and semi-leptonic decay modes of the top quark, that is: $pp \rightarrow t + N_R N_R \rightarrow bj\bar{j} + N_R N_R$, $bl\nu + N_R N_R$. We study the possibility of detecting a monotop signal with the full data set with 8 TeV centre of mass energy as well as in the future 14 TeV run.

A. LHC at 8 TeV: Hadronic mode.

To investigate the production of a single top quark with a large amount of missing energy at the LHC, we simulate collisions with the full 20 fb^{-1} of integrated luminosity at centre of mass energies of $\sqrt{s} = 8 \text{ TeV}$. For a hadronically decaying top, the only source of irreducible background is due to the production of an invisible decaying Z and three

jets, one tagged as a b -jet. The other dominant SM backgrounds consist of W plus jets, $t\bar{t}$ production, single top production, the production of two gauge bosons and QCD multijet production [20]. The latter are not simulated since their full implementation requires the use of data-driven methods. However, we implement a series of kinematic cuts that are useful in order to reduce this background.

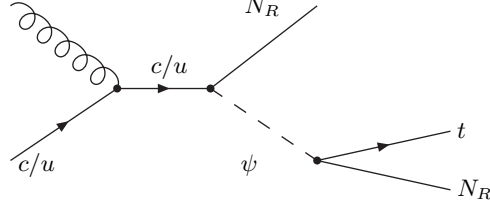


FIG. 12. Leading order Feynman diagram for monotop production at the LHC in association with missing transversed energy carried away by Majorana neutrino.

The dominant backgrounds are simulated at leading order using MadGraph 5 [62] and implement PYTHIA [63] for the parton showering and hadronization. We then reweight the events to include higher corrections when they are available. A k factor for $t\bar{t}$ production is obtained by normalizing the leading order (LO) inclusive production cross section to the next-to-next-to-leading order (NNLO) cross section calculated in [68]. For single top production we simulate $pp \rightarrow tj$, $pp \rightarrow t\bar{j}$, $pp \rightarrow tW$ and $pp \rightarrow t\bar{t}W$ and normalize the total cross section to the next-to-next-to-leading log threshold resummed result in [69]. For W and Z production we simulate the LO inclusive cross section and decay the gauge bosons leptonically. We then normalize the $pp \rightarrow W X \rightarrow l\nu X$ cross section to the NNLO result in [70] and the $pp \rightarrow Z X \rightarrow l^+l^- X$ in [71]. The LO order diboson production are normalized to their next-to-leading order predictions in [72]. The k -factors associated with the dominant backgrounds are summarized in Table I. The detector simulation is carried out with Delphes 3 [64].

	$W X, W \rightarrow l\nu_l$	$Z X, Z \rightarrow ll$	$t\bar{t}$	$tj + t\bar{t}W$	WZ	ZZ	WW
LO σ	10.78 nb	0.9416 nb	191.7 pb	100.16 pb	12.92 pb	4.90 pb	34.8 pb
NNLO σ	12.50 nb	1.13 nb	245.8 pb	114.95 pb	22.87 pb	7.94 pb	57.42
k -factor	1.16	1.20	1.28	1.15	1.77	1.62	1.65

TABLE I. k -factors for the leading SM backgrounds. The various next-to-leading results are summarized in the text.

In order to reduce the SM background we veto any events containing a lepton with $p_T > 10$ GeV and $|\eta| < 2.5$. This cuts have the effect of reducing the two most dominant backgrounds, $t\bar{t}$ and Wj for which either one top quark or the W boson decays leptonically. Furthermore, we identify b -jets as jets with a $p_T > 50$ GeV and consistent with the b -tagging information and light jets as those with $p_T > 30$ GeV. Both types of jets are required to lie within the detector geometry defined by $|\eta^j| < 2.5$. In Table II we show the simulated background processes with their cross sections and the total number of events generated.

Process	σ [pb]	$N_{generated}$
$Z + \text{jets}$	3.4×10^4	2.2×10^8
$W (\rightarrow l\nu) + \text{jets}$	2.28×10^4	5.0×10^7
$t\bar{t} + \text{jets}$	243.93	2.0×10^6
$tj + t\bar{t}W$	115.09	1.0×10^6
WW	57.30	5.0×10^5
WZ	22.87	5.0×10^5
ZZ	7.94	5.0×10^5

TABLE II. Cross sections normalized to their next-to-leading order results and the number of events generated for the leading SM background contributions at centre of mass energies of 8 TeV.

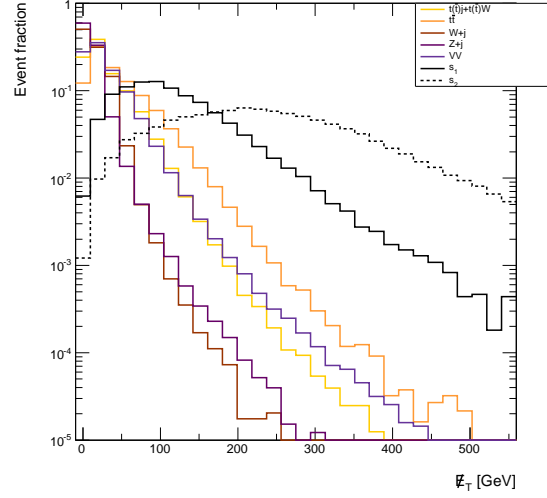


FIG. 13. Fraction of events as a function of the missing transverse energy, \cancel{E}_T . The black solid line represents a scenario within our framework where $m_\psi = 150$ GeV and $M_{N_R} = 80$ GeV while the dashed black line represents $m_\psi = 700$ GeV and $M_{N_R} = 210$ GeV. Both signals were generated using $(y_\psi^t, y_\psi^c, y_\psi^u) = (1, 0.001, 0.5)$.

One important feature of monotop production is that it contains a large amount of missing transverse energy. This is more prominent when the mass of the electroweak-singlet scalar is large compared to its decay products. We can see this in Figure 13, where compared to the background, events with $m_\psi = 700$ GeV and $M_{N_R} = 210$ GeV (dashed black line) and $(y_\psi^t, y_\psi^c, y_\psi^u) = (1, 0.001, 0.5)$, lie in the region where $\cancel{E}_T > 150$ GeV. This is also true for the low mass region (solid black line) where $m_\psi = 150$ GeV and $M_{N_R} = 80$ and $(y_\psi^t, y_\psi^c, y_\psi^u) = (1, 0.001, 0.5)$, though the distribution falls off more rapidly due to the off-shell nature of the scalar ψ . In addition, in order to properly reject more background events it is important to properly reconstruct the mass of the top quark. In particular, one will need to reject events without exactly one b -jet after implementing a b -tagging efficiency of 40 percent. The distribution for the number of b -jets is shown in Figure 14(a) and the number of light jets in Figure 14(b). Furthermore, to properly distinguish

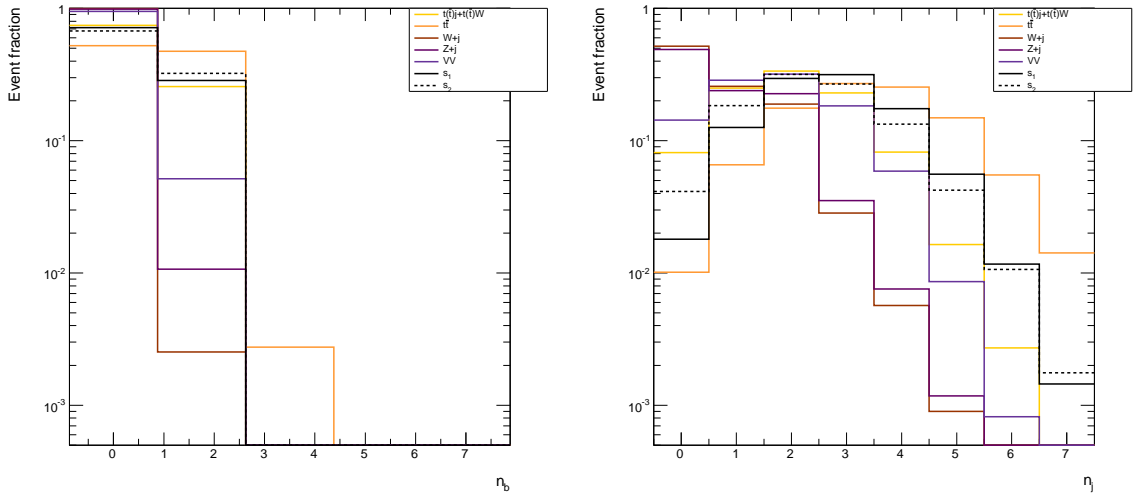


FIG. 14. Fraction of events as a function of the number of b -jets (left) and light jets (right). The signal was generated using the same parameter points as in Figure 13.

the signal from the background one has to distinguish amongst the different combinations of jets from the one arising from the hadronic decay of a top quark and consistent with the b -tagging information. We do this by implementing

a hadronic top χ^2 variable used in [65]. For each triplet of jets out of the 7 leading light jets and the leading b -jet a χ^2 variable is constructed as:

$$\chi^2 = \frac{(M_{bj_1j_2} - M_{top})^2}{\sigma_{bj_1j_2}^2} + \frac{(M_{j_1j_2} - M_W)^2}{\sigma_{j_1j_2}^2}, \quad (47)$$

where $M_{bj_1j_2}$ is the mass of the three-jet system, $M_{j_1j_2}$ is the mass of the two jet system, $M_{top} = 174$ GeV the pole mass of the top quark, and $M_W = 80.4$ GeV the mass of the W boson. The variables $\sigma_{bj_1j_2}$ and $\sigma_{j_1j_2}$ are the uncertainties on the masses obtained after implementing a jet energy resolution of 5%. In Figure 15 we show the cross section as a function of the reconstructed top quark mass that minimizes the χ^2 variable after requiring exactly one b -jet and no charged leptons. One can see that the majority of signal and background events are consistent with the hadronic decay of a top quark. Therefore, restricting this variable, applying an appropriate MET cut and requiring the absence of a charged lepton can significantly reduce the $t\bar{t}$ and single-top backgrounds when the top quark decays semileptonically and completely suppresses events originating from W and Z plus jets.

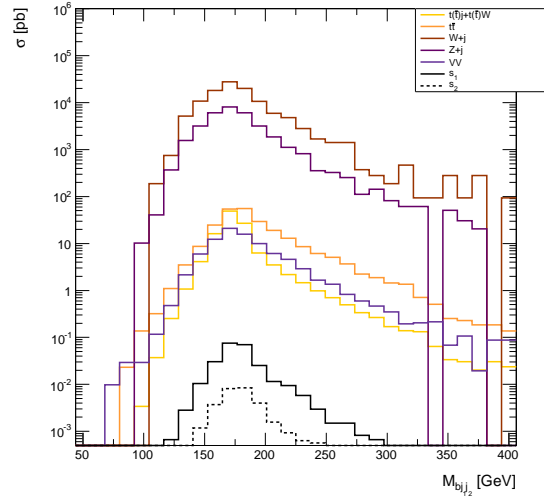


FIG. 15. Cross section as a function of the reconstructed top quark mass after requiring exactly one b -jet and no charged leptons and that minimizes the χ^2 variable defined in Equation 47. The signal was generated using the same parameter points as in Figure 13.

SM background	$N^{\# > 90 \text{ GeV}} (\sigma \text{ [pb]})$	$N^{\# > 200 \text{ GeV}} (\sigma \text{ [pb]})$
$W (\rightarrow l\nu) + \text{jets}$	1925 (0.096)	137 (6.83×10^{-3})
$Z + \text{jets}$	420 (0.021)	< 3 ($< 1.54 \times 10^{-4}$)
$t\bar{t} + \text{jets}$	11080 (0.55)	344 (0.017)
$t j + t W$	892 (0.044)	37 (1.84×10^{-3})
WW	17 (8.60×10^{-5})	< 1 ($< 5.73 \times 10^{-5}$)
WZ	22 (1.12×10^{-3})	2 (9.15×10^{-5})
ZZ	11 (5.72×10^{-4})	1 (4.76×10^{-5})

TABLE III. Number of expected events, N , with 20 fb^{-1} of integrated luminosity and cross section in the two signal regions specified by the amount of MET (> 90 , > 200 GeV) and after applying the following cuts: $n_b = 1$, $n_j = 2$ or 3 , a $\chi^2 < 5$, $50 < M_{j_1j_2}^{\chi^2_{\min}} < 105$ GeV and $140 < M_{bj_1j_2}^{\chi^2_{\min}} < 195$ GeV.

To analyze the monotop discovery reach within our framework we look at parameter points that can yield a large $p p \rightarrow N_R \psi$ production rate with a large branching ratio $\psi \rightarrow N_R t$. We choose to scan over the coloured electroweak-singlet and Majorana neutrino masses using two benchmark points $(y_\psi^t, y_\psi^c, y_\psi^u) = (1, 0.001, 0.5), (0.65, 0.001, 1)$. In the scans we have set the y_ψ^c coupling close to zero to suppress the constraints arising from $D^0 - \bar{D}^0$ oscillations. A large y_ψ^t coupling is chosen since it yields natural values for neutrino masses and avoids the constraints arising from rare

decays of the muon. From the above considerations we implement two different hadronic monotop search strategies based on the amount of missing energy design to increase the sensitivity to the low and high m_ψ regions. We define a loose cut region by imposing $\cancel{E}_T > 90$ GeV and a tight cut region by $\cancel{E}_T > 200$ GeV.

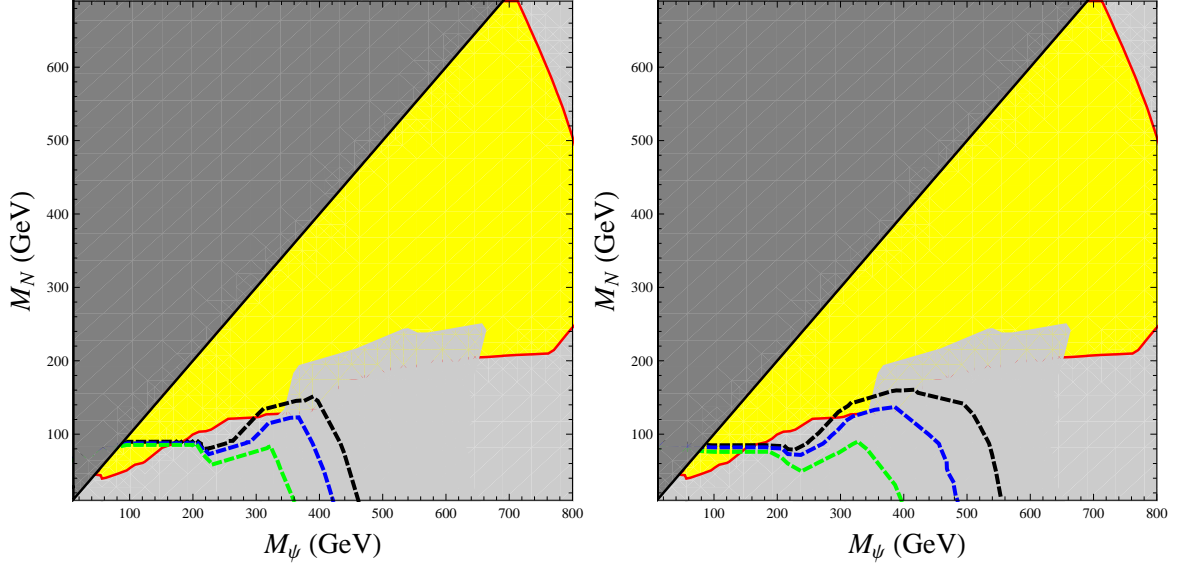


FIG. 16. LHC reach with 20 fb^{-1} at 8 TeV of our hadronic monotop signal using $(y_\psi^t, y_\psi^c, y_\psi^u) = (1, 0.001, 0.5)$ after applying all the cuts described in the text with $\cancel{E}_T > 90$ GeV (left) and $\cancel{E}_T > 200$ GeV (right). We show three regions where our monotop signal can reach a significance, $s = S/\sqrt{S+B}$, of two, three and five sigma depicted by the dashed black, blue and green lines respectively.

Using the information from Figures 13-15 we implement the following universal cuts to suppress the SM backgrounds: Demand exactly one b -jet and 2 or 3 light jets; a hadronic χ^2 variable below 5, and a reconstructed two-jet system consistent with the mass of the W boson. The number of background events in both MET regions is given in Table III. In Figures 16(a) and 16(b) we show the allowed region of parameter space after all constraints have been taken into consideration (light and dark grey regions) in the $m_\psi - M_{N_R}$ plane for the loose cut criteria and $(y_\psi^t, y_\psi^c, y_\psi^u) = (1, 0.001, 0.5)$. The yellow region is allowed but the dark matter candidate annihilates too efficiently to account for the dark matter relic abundance; while the red solid line is consistent with $\Omega_{DM} h^2 = 0.1199 \pm 0.0027$ [6]. In the figure we show three regions where our monotop signal can reach a significance, $s = S/\sqrt{S+B}$, of two, three and five sigma depicted by the dashed black, blue and green lines respectively. It is clear from the figures that a larger MET cut increases the sensitivity to the high m_ψ region but it quickly enters the region excluded by stop pair production. Regions of $m_\psi > 600$ GeV have very small cross sections and are difficult to probe with the LHC's current data set. The monotop production cross section can be enhanced by an increase in y_ψ^u . We show our results with $(y_\psi^t, y_\psi^c, y_\psi^u) = (0.65, 0.001, 1)$ in Figures 17(a) and 17(b) for the loose and tight MET cuts respectively. Unlike our previous case, the low mass region here is more tightly constrained due to monojet searches but the high mass region has an increased sensitivity. In addition, within this benchmark, the region with a heavy Majorana neutrino accompanied by a moderately heavy coloured electroweak-singlet scalar is more constrained from stop pair production searches due to the enhancement in the $tt + \text{MET}$ production cross section coming from Figure 9(a).

Only a small region of parameter space can be probed since the most promising set of cuts remains plagued by the all-hadronic $t\bar{t}$ SM background. One can try to reduce this background, as well as QCD multijet events, using data estimates. This was done in [73], where they search for direct production of the stop squark in the all hadronic $t\bar{t} + \cancel{E}_T$ final state. A set of cuts in the angular separation between the leading light jet and the MET as well as the leading b -jet and the MET, $\Delta\phi(p_{T(j,b)j}, \cancel{E}_T) > \pi/5$, was sufficient to suppress all of the $t\bar{t}$ background and the single-top background for a hadronically decaying top quark, and potentially a large fraction of QCD multijet events, but at the cost of losing most of the sensitivity to the allowed region of parameter space. The results are shown in Figure 18(a) for $(y_\psi^t, y_\psi^c, y_\psi^u) = (1, 0.001, 0.5)$ and Figure 18(b) for $(y_\psi^t, y_\psi^c, y_\psi^u) = (0.65, 0.001, 1)$ requiring $\cancel{E}_T > 200$ GeV and similarly in Figures 19(a) and 19(b) for $\cancel{E}_T > 90$. We conclude that due to the small monotop production cross sections and unlike the resonant production of a coloured electroweak-singlet scalar [20, 22, 23], a hadronic monotop search would be very challenging with the full 8 TeV data set and can at best probe the low m_ψ for not too large y_ψ^u , avoiding the strong monojet constraints.

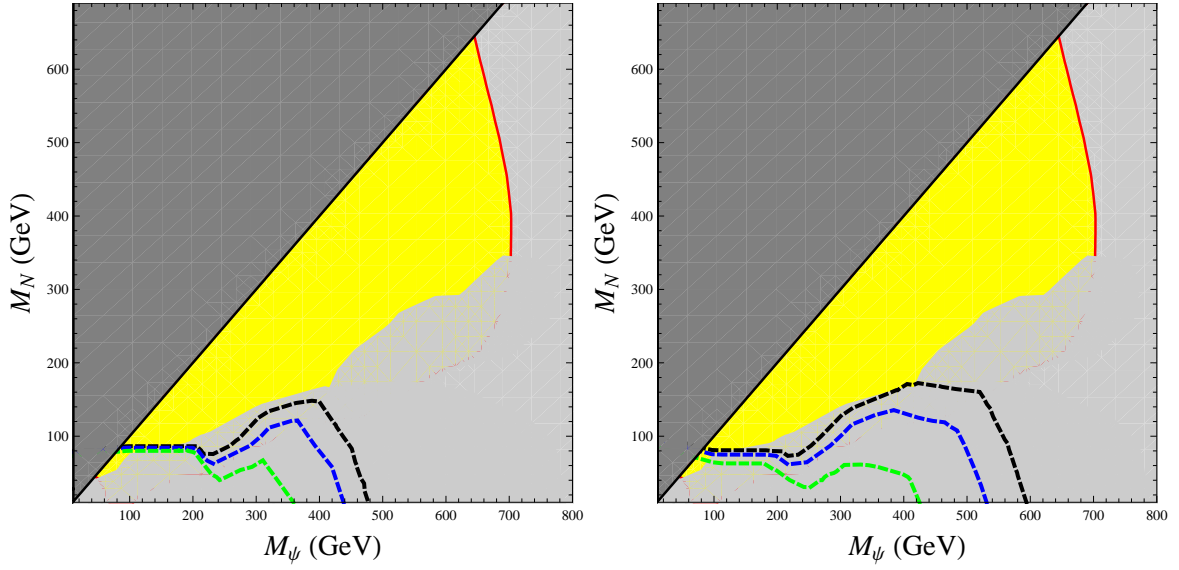


FIG. 17. Same as in Figure 16 with $(y_\psi^t, y_\psi^c, y_\psi^u) = (0.65, 0.001, 1)$.

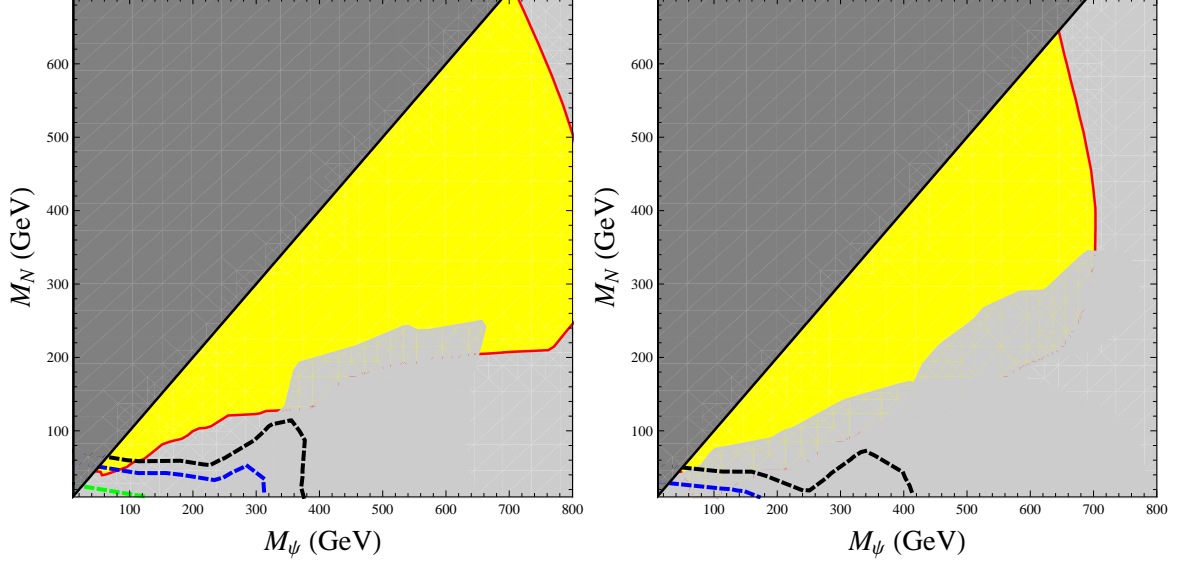


FIG. 18. Same as in Figure 16 with $(y_\psi^t, y_\psi^c, y_\psi^u) = (1, 0.001, 0.5)$ (left) and $(y_\psi^t, y_\psi^c, y_\psi^u) = (0.65, 0.001, 1)$ and $\cancel{E}_T > 200$ GeV. An additional cut was applied on the angular separation between the leading light jet and the MET and the leading b -jet and the MET, $\Delta\phi(p_{T(j,b)}, \cancel{E}_T) > \pi/5$ to suppress the all-hadronic $t\bar{t}$ and multijet backgrounds.

B. LHC at 8 TeV: Leptonic mode.

In the previous section we analyzed the prospect of probing the allowed region of parameter space by implementing a search strategy which tags a singly produced top quark through its hadronic decay mode. We saw that such feat is very challenging due to the small monotop production cross sections together with the presence of large QCD multijet and the all-hadronic $t\bar{t}$ backgrounds. In what follows we implement a monotop search strategy developed in [28], where one tags the top quark through its semi-leptonic decay mode. The authors show that the key kinematic variable used to suppress most of the SM backgrounds is the transverse mass of the charged lepton, M_T , which has an endpoint at the mass of the W boson. In addition, they show that QCD multijet and the all-hadronic $t\bar{t}$ backgrounds can be rejected by applying a high p_T jet veto which suppresses the QCD missing energy that arises from misreconstructed jets. Furthermore, the authors argue that this search strategy should lead to a signal significance which can be

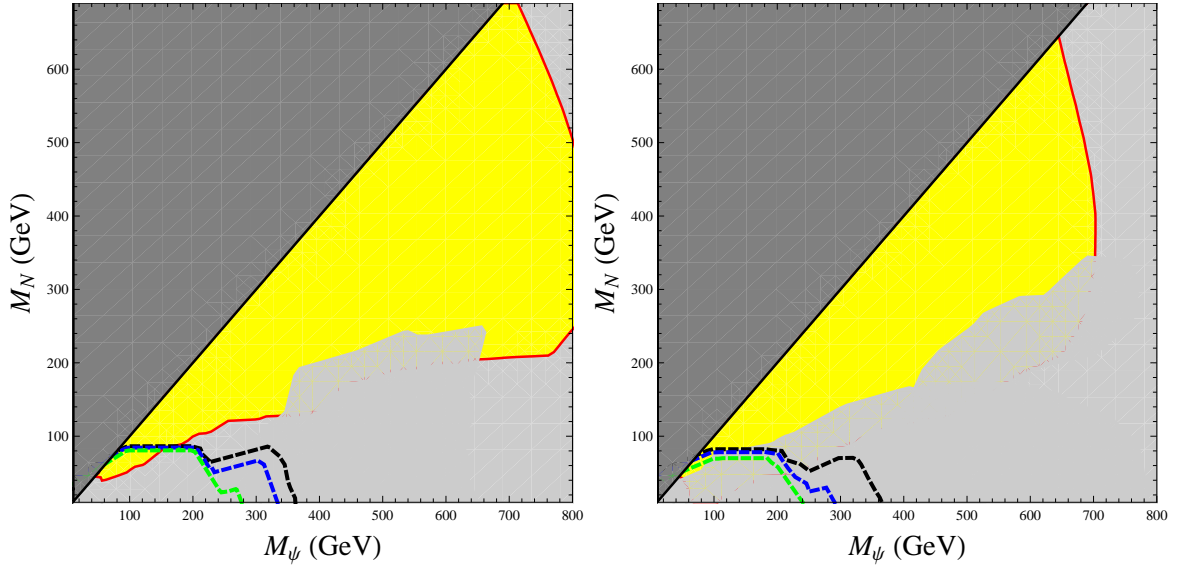


FIG. 19. Same as in Figure 18 with $E_T > 90$ GeV.

probed with the current LHC data set even if the production cross sections are two orders of magnitude below their benchmark scenario.

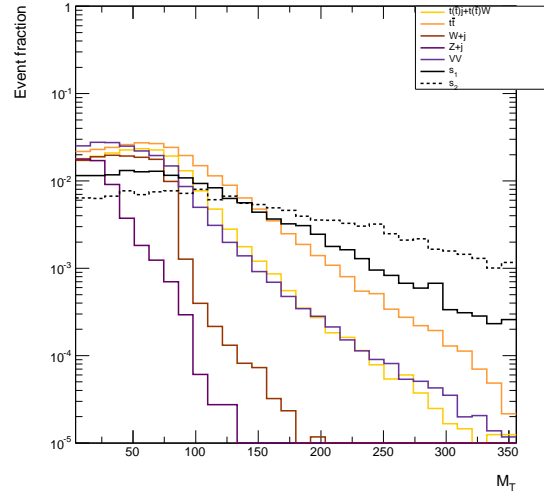


FIG. 20. Fraction of events as a function of the lepton's transverse mass, M_T . The black solid line represents a scenario within our framework where $m_\psi = 150$ GeV and $M_{N_R} = 80$ GeV while the dashed black line represents $m_\psi = 700$ GeV and $M_{N_R} = 210$ GeV. Both signals were generated using $(y_\psi^t, y_\psi^c, y_\psi^u) = (1, 0.001, 0.5)$.

Unlike the hadronic mode, we pre-select events by requiring one charged lepton with $p_T > 20$ GeV and $|\eta| < 2.5$ in addition to the presence of a b -jet with $p_T > 20$ GeV and $|\eta| < 2.5$. Using Figures 13 and 20, we implement two sets of cuts on the MET and M_T to enhance the sensitivity to the low and high m_ψ regions. Furthermore, in order to suppress the QCD multijet background, in samples with one jet, we exclude any event where the $p_{T,j} > 70, 120$ GeV for the two sets of cuts respectively. In Table IV we show the number of expected events and cross section for the SM backgrounds for two sets of cuts. One can see that the Z +jets background is negligible in both cases, while a high MET cut and a large jet p_T veto significantly reduces the $t\bar{t}$ and W +jets backgrounds.

In Figures 21(a) and 21(b) we show the allowed region of parameter space after all constraints have been taken into consideration (light and dark grey regions) in the $m_\psi - M_{N_R}$ plane for the two sets of cuts using $(y_\psi^t, y_\psi^c, y_\psi^u) = (1, 0.001, 0.5)$. We can see that the semi-leptonic mode yields similar results to the hadronic mode after cuts to

SM background	$N^{\cancel{E}>90 \text{ GeV}, M_T>110 \text{ GeV}} (\sigma [\text{pb}])$	$N^{\cancel{E}>200 \text{ GeV}, M_T>120 \text{ GeV}} (\sigma [\text{pb}])$
$W (\rightarrow l\nu) + \text{jets}$	212 (0.011)	$< 7 (< 3.41 \times 10^{-4})$
$Z + \text{jets}$	$< 3 (< 1.54 \times 10^{-4})$	$< 3 (< 1.54 \times 10^{-4})$
$t\bar{t} + \text{jets}$	1327 (0.066)	49 (2.46×10^{-3})
$t j + t W$	242 (0.012)	$< 2 (< 1.15 \times 10^{-4})$
WW	2 (1.15×10^{-4})	$< 1 (5.73 \times 10^{-5})$
WZ	1 (6.86×10^{-5})	*** ($< 2.29 \times 10^{-5}$)
ZZ	*** ($< 7.94 \times 10^{-6}$)	*** ($< 7.94 \times 10^{-6}$)

TABLE IV. Number of expected events, N , with 20 fb^{-1} of integrated luminosity and cross section in the two signal regions specified by the amount of MET ($> 90, > 200 \text{ GeV}$) and charged lepton's transverse mass, M_T ($> 110, 120 \text{ GeV}$) and after applying the following cuts: $n_b = 1, n_j = 0$ or 1 .

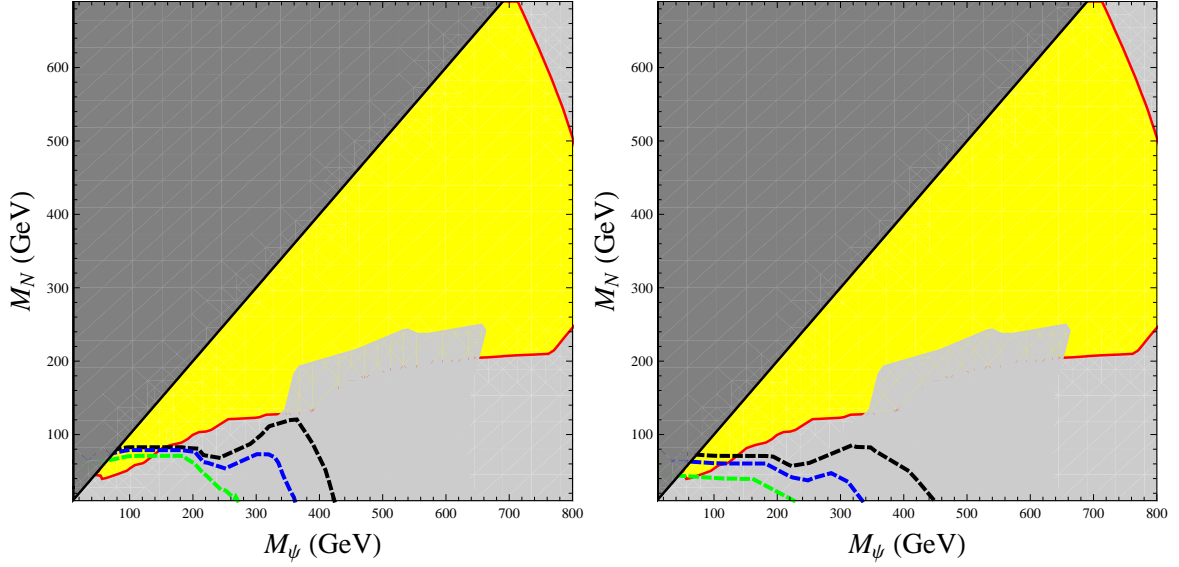


FIG. 21. LHC reach with 20 fb^{-1} at 8 TeV of our semileptonic monotop signal using $(y_\psi^t, y_\psi^c, y_\psi^u) = (1, 0.001, 0.5)$ after applying all the cuts described in the text with $\cancel{E}_T, M_T > 90, 110 \text{ GeV}$ (left) and $\cancel{E}_T, M_T > 200, 120 \text{ GeV}$ (right). We show three regions where our monotop signal can reach a significance, $s = S/\sqrt{S+B}$, of two, three and five sigma depicted by the dashed black, blue and green lines respectively.

suppress the all-hadronic $t\bar{t}$ and multijet backgrounds are applied, Figures 18(a)-19(a), and with a larger significance in the low m_ψ region. Similarly, for $(y_\psi^t, y_\psi^c, y_\psi^u) = (0.65, 0.001, 1)$ in Figures 22(a) and 22(b), but again here the region that can be probed with a semi-leptonic monotop search is ruled out by monojet searches. Since we can more easily reject the all-hadronic $t\bar{t}$ and QCD multijet backgrounds by tagging the monotop through its semi-leptonic decay, in the next section we apply the above search strategy to the LHC running at energies of 14 TeV , and we look at the possibility of probing our model with 30 and 300 fb^{-1} of integrated luminosities.

C. LHC at 14 TeV

In this section we analyze the LHC reach of our monotop signal at 14 TeV centre of mass energies with 30 and 300 fb^{-1} of integrated luminosities. We give an estimate of the SM backgrounds using the k -factors introduced in Table I to account for the higher order QCD corrections. The normalized cross sections and the number of events generated are given in Table V. In the previous sections we saw that both the hadronic mode, post- $t\bar{t}$ all-hadronic cuts, and the semi-leptonic mode yielded comparable sensitivities to the monotop signal. However, since in the leptonic mode the QCD multijet background component can be safely neglected, we choose to approach the 14 TeV analysis requiring an isolated lepton in the final state.

In our analysis the focus is in the scenario where $(y_\psi^t, y_\psi^c, y_\psi^u) = (1, 0.001, 0.5)$, since this benchmark will not be

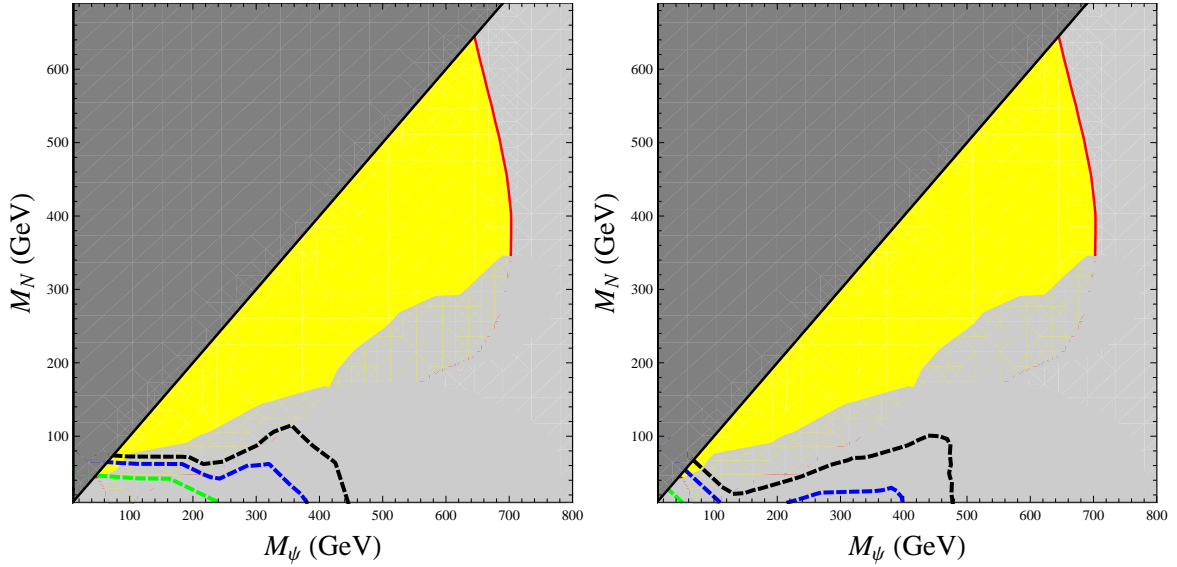


FIG. 22. Same as in Figure 21 with $(y_\psi^t, y_\psi^c, y_\psi^u) = (0.65, 0.001, 1)$.

Process	σ [pb]
$W + \text{jets}$	2.19×10^5
$Z + \text{jets}$	6.66×10^4
$t\bar{t} + \text{jets}$	1052.93
$tj + tW$	347.42
WW	119.84
WZ	48.87
ZZ	17.09

TABLE V. Cross sections normalized to their next-to-leading order results for the leading SM background contributions at centre of mass energies of 14 TeV. The cross sections are normalized using the k -factors introduced in Table I.

in much tension with dark matter direct detection constraints. In the previous subsection, we showed that the full data set at $\sqrt{s} = 8$ TeV was not enough to probe the parameter space using the semi-leptonic decay mode of the top quark. However, we saw that a large enough cut on the MET was enough to suppress the W and Z plus jets backgrounds. This was due to the low acceptance rate from demanding a b -jet and an isolated lepton in the final state. The suppression of the W plus jets background component was also due to a cut on the transverse mass of the charged lepton, M_T . At energies of $\sqrt{s} = 14$ TeV, the same behaviour is observed if one keeps events with a high enough MET. Therefore, in our analysis we apply the cuts used to enhance the sensitivity of the search to the high m_ψ region:

$$\cancel{E}_T > 200 \text{ GeV}, \quad M_T > 120 \text{ GeV}. \quad (48)$$

In addition, we require events to contain up to one jet with $p_T < 120$ GeV to suppress the QCD multijet SM background which we do not simulate. The signal cross section together with the two dominant backgrounds, $t\bar{t}$ and $tj + tW$, are shown in Table VI. The signal corresponds to a coloured electroweak-singlet scalar with mass $m_\psi = 700$ GeV and a Majorana neutrino with mass $M_{N_R} = 210$ GeV. In Figures 23(a) and 23(b) we show the signal significance in the $m_\psi - M_{N_R}$ plane using 30 fb^{-1} and 300 fb^{-1} of integrated luminosities respectively. Contours of two, three and five sigma are depicted by the dashed black, blue and green lines respectively. Compared to the scenario depicted in Figure 21(b), the increase in energy from 8 to 14 TeV already shows that the LHC will potentially begin to probe this framework very early during run 2. However, an order of magnitude increase in the luminosity will probe the allowed region of parameter space for Majorana neutrino masses below ~ 400 GeV.

Even though the above analysis has been carried out by tagging the semi-leptonic decay mode of the top quark, one can equally tag the hadronic decay mode and apply similar cuts as those mentioned at the beginning of this section. However, the all-hadronic and QCD multijet backgrounds do represent a problem in accurately taking into account all

\mathcal{L} [fb $^{-1}$]	$\sigma(t\bar{t} + \text{jets})$ [pb], N	$\sigma(tj + tW)$ [pb], N	σ_{signal} [pb], N
30	6.31×10^{-3} , 189	1.39×10^{-3} , 42	6.85×10^{-4} , 21
300	1892	417	205

TABLE VI. Number of expected events, N , with 30 and 300 fb $^{-1}$ of integrated luminosities and cross section at $\sqrt{s} = 14$ TeV for the two dominant SM backgrounds specified after applying the cuts mentioned in the text. The signal strength is also shown for $m_\psi = 700$ GeV and $M_{N_R} = 210$ GeV.

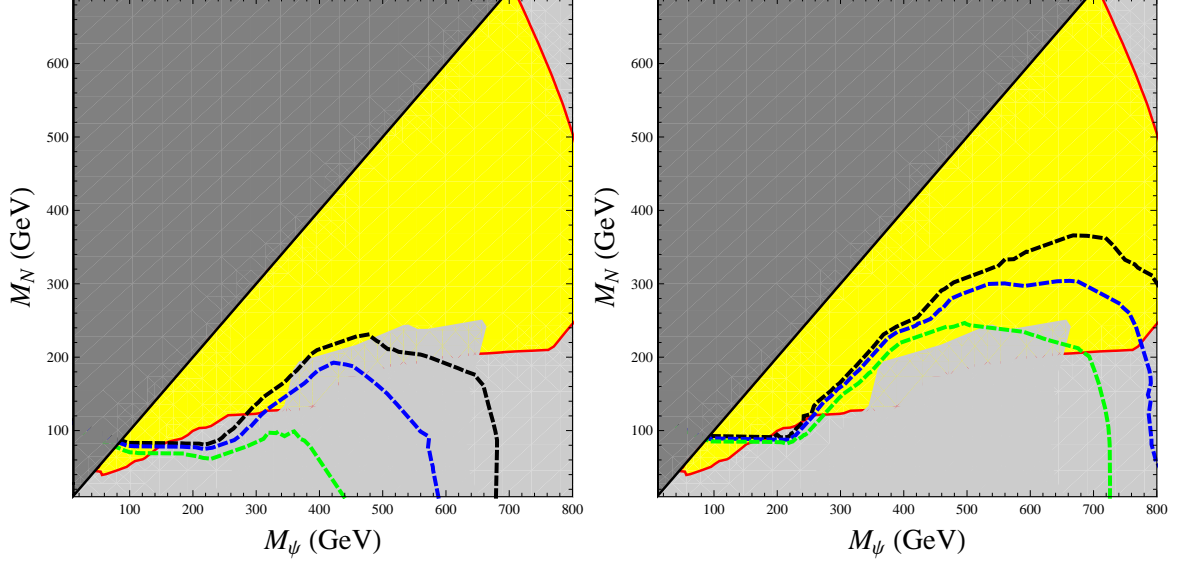


FIG. 23. LHC reach with 30 (left) fb $^{-1}$ and 300 fb $^{-1}$ (right) at 14 TeV of our semileptonic monotop signal using $(y_\psi^t, y_\psi^c, y_\psi^u) = (1, 0.001, 0.5)$ and after applying all the cuts described in the text. The three regions where our monotop signal can reach a significance, $s = S/\sqrt{S+B}$, of two, three and five sigma are depicted by the dashed black, blue and green lines respectively.

SM backgrounds. Simulating these backgrounds will require the combined efforts from experimentalists and theorists alike. Nonetheless, one can start to better discriminate the signal from the well established SM backgrounds by tagging boosted tops. Within our framework, at $\sqrt{s} = 14$ TeV, the production of heavy coloured electroweak-singlet scalars leads to boosted tops provided that the mass of the Majorana neutrino is not very large. This is particularly interesting since this region of parameter space is consistent with the relic abundance of dark matter in the universe. In Figure 24 we show the fraction of events as a function of the transverse momentum of the reconstructed top quark, $p_{T,top}$. The momentum corresponds to the combination of jets with minimizes the χ^2 variable introduced in Equation 47. The black dashed line corresponds to the signal with $m_\psi = 700$ GeV and $M_{N_R} = 210$ GeV. The study of boosted tops and how they are tagged is an active field of research [74–79] and it would be very interesting to see its effects on models that predict a monotop signal at large centre of mass energies, together with a full implementation and treatment of the QCD multijet background.

VIII. DISCUSSION

In this study we have generalized the model introduced in [33], coupling all three generations of right-handed up-type quarks to a Majorana neutrino and a coloured electroweak-singlet scalar. Within this framework, the dark matter relic abundance can match the latest experimental results over a wide range of couplings $y_\psi^{t,c,u}$. However, we saw that very large values of y_ψ^u can be in disagreement with limits obtained from direct dark matter searches. In particular, the model is mainly constrained by spin dependent interactions between the dark matter and nuclei. The constraints are larger when the coloured electroweak-singlet scalar is in resonance with the Majorana neutrino. Furthermore, the possibility of radiatively generating Majorana masses for the active neutrinos is mainly dependent on y_ψ^t since the contributions from the up and charm quarks are proportional to their masses. Natural neutrino masses are possible over the whole range of y_ψ^t values. However, constraints from rare decays such as $\mu \rightarrow e\gamma$ prefer large values of y_ψ^t . In addition, D -meson oscillations tend to constrain the product $y_\psi^u y_\psi^c$.

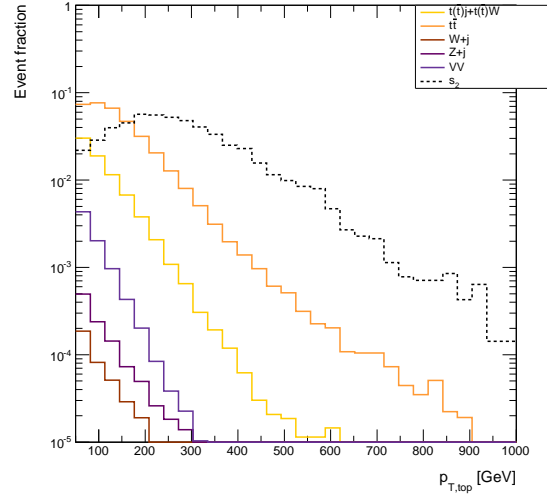


FIG. 24. Fraction of events as a function of the transverse momentum of the reconstructed top quark, $p_{T,top}$. The dashed black line represents a scenario within our framework where $m_\psi = 700$ GeV and $M_{NR} = 210$ GeV. Both signals were generated using $(y_\psi^t, y_\psi^c, y_\psi^u) = (1, 0.001, 0.5)$.

We have implemented collider searches for monojets and multijets in association with missing transverse energy. In addition, it was seen that searches for scalar top pair production can further exclude a wide region of the parameter space. To analyze the impact of these searches, we have applied the constraints to three benchmark scenarios. The benchmark scenarios all have a large value of y_ψ^t to evade rare decay bounds and small value of y_ψ^c to avoid constraints from flavour oscillations. Three values of y_ψ^u ranging from 0.1 – 1 are considered. This coupling is varied mainly because we study the production of a single top quark in association with missing transverse energy, which in this framework, has as the main production mode quark-gluon fusion. This production mode is enhanced for large values of y_ψ^u , however, the parameter region corresponding to large y_ψ^u is highly constrained by monojet + MET searches.

We have analyzed the monotop production in both the hadronic and semi-leptonic decay modes of the top quark and saw that with the current $\sqrt{s} = 8$ TeV data set a monotop search does not probe the allowed region of parameter space. The situation changes at $\sqrt{s} = 14$ TeV, where an approximate calculation puts this model within the reach of the LHC with 300 fb^{-1} of integrated luminosity. Future work may want to consider better top quark reconstruction techniques to better discriminate the SM background. In particular, tagging boosted tops can be used to better probe models that predict a monotop signature with 14 TeV centre of mass energies.

ACKNOWLEDGEMENTS

John Ng and ADP would like to thank Estefania Coluccio Leskow, Travis Martin, Kristian L. McDonald, and David Morrissey for useful discussions and essential feedback regarding the progress of this work. This work is supported in parts by the National Science and Engineering Council of Canada.

-
- [1] L. Bergstrom, Rept. Prog. Phys. **63**, 793 (2000) [hep-ph/0002126].
 - [2] G. Bertone, D. Hooper and J. Silk, Phys. Rept. **405**, 279 (2005) [hep-ph/0404175].
 - [3] K. G. Begeman, A. H. Broeils and R. H. Sanders, Mon. Not. Roy. Astron. Soc. **249**, 523 (1991).
 - [4] M. Bradac, D. Clowe, A. H. Gonzalez, P. Marshall, W. Forman, C. Jones, M. Markevitch and S. Randall *et al.*, Astrophys. J. **652**, 937 (2006) [astro-ph/0608408].
 - [5] C. L. Bennett *et al.* [WMAP Collaboration], Astrophys. J. Suppl. **208**, 20 (2013) [arXiv:1212.5225 [astro-ph.CO]].
 - [6] P. A. R. Ade *et al.* [Planck Collaboration], arXiv:1303.5076 [astro-ph.CO].
 - [7] E. Behnke, J. Behnke, S. J. Brice, D. Broemmelsiek, J. I. Collar, P. S. Cooper, M. Crisler and C. E. Dahl *et al.*, Phys. Rev. Lett. **106**, 021303 (2011) [arXiv:1008.3518 [astro-ph.CO]].

- [8] S. Archambault, F. Aubin, M. Auger, E. Behnke, B. Beltran, K. Clark, X. Dai and A. Davour *et al.*, Phys. Lett. B **682**, 185 (2009) [arXiv:0907.0307 [hep-ex]].
- [9] M. Felizardo, T. A. Girard, T. Morlat, A. C. Fernandes, A. R. Ramos, J. G. Marques, A. Kling and J. Puibasset *et al.*, Phys. Rev. Lett. **108**, 201302 (2012) [arXiv:1106.3014 [astro-ph.CO]].
- [10] J. Angle, E. Aprile, F. Arneodo, L. Baudis, A. Bernstein, A. Bolozdynya, L. C. C. Coelho and C. E. Dahl *et al.*, Phys. Rev. Lett. **101**, 091301 (2008) [arXiv:0805.2939 [astro-ph]].
- [11] E. Aprile *et al.* [XENON100 Collaboration], Phys. Rev. Lett. **111**, 021301 (2013) [arXiv:1301.6620 [astro-ph.CO]].
- [12] Z. Ahmed *et al.* [CDMS-II Collaboration], Phys. Rev. Lett. **106**, 131302 (2011) [arXiv:1011.2482 [astro-ph.CO]].
- [13] Z. Ahmed *et al.* [CDMS-II Collaboration], Science **327**, 1619 (2010) [arXiv:0912.3592 [astro-ph.CO]].
- [14] E. Aprile *et al.* [XENON100 Collaboration], Phys. Rev. Lett. **109**, 181301 (2012) [arXiv:1207.5988 [astro-ph.CO]].
- [15] D. S. Akerib *et al.* [LUX Collaboration], arXiv:1310.8214 [astro-ph.CO].
- [16] [ATLAS Collaboration], ATLAS-CONF-2012-147.
- [17] The ATLAS collaboration, ATLAS-CONF-2013-047.
- [18] [CMS Collaboration], CMS-PAS-EXO-12-048.
- [19] [CMS Collaboration], CMS-PAS-SUS-10-011.
- [20] J. Andrea, B. Fuks and F. Maltoni, Phys. Rev. D **84**, 074025 (2011) [arXiv:1106.6199 [hep-ph]].
- [21] T. Aaltonen *et al.* [CDF Collaboration], Phys. Rev. Lett. **108**, 201802 (2012) [arXiv:1202.5653 [hep-ex]].
- [22] J. Wang, C. S. Li, D. Y. Shao and H. Zhang, Phys. Rev. D **86**, 034008 (2012) [arXiv:1109.5963 [hep-ph]].
- [23] J. -L. Agram, J. Andrea, M. Buttignol, E. Conte and B. Fuks, Phys. Rev. D **89**, 014028 (2014) [arXiv:1311.6478 [hep-ph]].
- [24] E. Alvarez and E. C. Leskow, Phys. Rev. D **86**, 114034 (2012) [arXiv:1209.4354 [hep-ph]].
- [25] J. Drobnak, A. L. Kagan, J. F. Kamenik, G. Perez and J. Zupan, Phys. Rev. D **86**, 094040 (2012) [arXiv:1209.4872 [hep-ph]].
- [26] T. Li and Q. Shafi, Phys. Rev. D **83**, 095017 (2011) [arXiv:1101.3576 [hep-ph]].
- [27] C. D. Froggatt and H. B. Nielsen, Nucl. Phys. B **147**, 277 (1979).
- [28] E. Alvarez, E. C. Leskow, J. Drobnak and J. F. Kamenik, Phys. Rev. D **89**, 014016 (2014) [arXiv:1310.7600 [hep-ph]].
- [29] A. Kumar, J. N. Ng, A. Spray and P. T. Winslow, Phys. Rev. D **88**, 075012 (2013) [arXiv:1308.3712 [hep-ph]].
- [30] E. L. Berger, B. W. Harris and Z. Sullivan, Phys. Rev. Lett. **83**, 4472 (1999) [hep-ph/9903549].
- [31] E. L. Berger, B. W. Harris and Z. Sullivan, Phys. Rev. D **63**, 115001 (2001) [hep-ph/0012184].
- [32] N. Desai and B. Mukhopadhyaya, JHEP **1010**, 060 (2010) [arXiv:1002.2339 [hep-ph]].
- [33] J. N. Ng and A. de la Puente, Phys. Lett. B **727**, 204 (2013) [arXiv:1307.2606].
- [34] Y. Bai and J. Berger, JHEP **1311**, 171 (2013) [arXiv:1308.0612 [hep-ph]].
- [35] S. Chang, R. Edezhath, J. Hutchinson and M. Luty, arXiv:1307.8120 [hep-ph].
- [36] H. An, L. -T. Wang and H. Zhang, arXiv:1308.0592 [hep-ph].
- [37] A. DiFranzo, K. I. Nagao, A. Rajaraman and T. M. P. Tait, JHEP **1311**, 014 (2013) [arXiv:1308.2679 [hep-ph]].
- [38] M. Garny, A. Ibarra, S. Rydbeck and S. Vogl, arXiv:1403.4634 [hep-ph].
- [39] E. W. Kolb and M. S. Turner, Front. Phys. **69**, 1 (1990).
- [40] J. D. Wells, hep-ph/9404219.
- [41] G. Belanger, F. Boudjema, P. Brun, A. Pukhov, S. Rosier-Lees, P. Salati and A. Semenov, Comput. Phys. Commun. **182**, 842 (2011) [arXiv:1004.1092 [hep-ph]].
- [42] N.D. Christensen and C. Duhr, Comput. Phys. Commun. **180**, 1614 (2009)
- [43] K. Griest and D. Seckel, Phys. Rev. D **43**, 3191 (1991).
- [44] P. Agrawal, Z. Chacko, C. Kilic and R. K. Mishra, arXiv:1003.1912 [hep-ph].
- [45] G. K. Mallot, Int. J. Mod. Phys. A **15S1**, 521 (2000) [eConf C **990809**, 521 (2000)] [hep-ex/9912040].
- [46] DMtools. <http://dmtools.brown.edu/>
- [47] L. M. Krauss, S. Nasri and M. Trodden, Phys. Rev. D **67**, 085002 (2003) [hep-ph/0210389].
- [48] A. Ahriche, C. -S. Chen, K. L. McDonald and S. Nasri, arXiv:1404.2696 [hep-ph].
- [49] E. Bertuzzo, P. A. N. Machado and R. Z. Funchal, arXiv:1302.0653 [hep-ph].
- [50] J. Adam *et al.* [MEG Collaboration], Phys. Rev. Lett. **107**, 171801 (2011) [arXiv:1107.5547 [hep-ex]].
- [51] Y. Amhis *et al.* [Heavy Flavor Averaging Group Collaboration], arXiv:1207.1158 [hep-ex].
- [52] R. Aaij *et al.* [LHCb Collaboration], Phys. Rev. Lett. **111** (2013) 101805 [arXiv:1307.5024 [hep-ex]].
- [53] S. Chatrchyan *et al.* [CMS Collaboration], Phys. Rev. Lett. **111**, 101804 (2013) [arXiv:1307.5025 [hep-ex]].
- [54] G. Aad *et al.* [ATLAS Collaboration], Phys. Lett. B **712**, 351 (2012) [arXiv:1203.0529 [hep-ex]].
- [55] E. Golowich, J. Hewett, S. Pakvasa and A. A. Petrov, Phys. Rev. D **76**, 095009 (2007) [arXiv:0705.3650 [hep-ph]].
- [56] [ATLAS Collaboration], ATLAS-CONF-2013-014.
- [57] [CMS Collaboration], CMS-PAS-HIG-13-005.
- [58] W. -F. Chang, J. N. Ng and J. M. S. Wu, Phys. Rev. D **86**, 033003 (2012) [arXiv:1206.5047 [hep-ph]].
- [59] [ATLAS Collaboration], ATLAS-CONF-2013-012.
- [60] [CMS Collaboration], CMS-PAS-HIG-13-001.
- [61] R. Mahbubani, M. Papucci, G. Perez, J. T. Ruderman and A. Weiler, Phys. Rev. Lett. **110**, 151804 (2013) [arXiv:1212.3328 [hep-ph]].
- [62] J. Alwall, M. Herquet, F. Maltoni, O. Mattelaer and T. Stelzer, JHEP **1106**, 128 (2011) [arXiv:1106.0522 [hep-ph]].
- [63] T. Sjostrand, S. Mrenna and P. Z. Skands, JHEP **0605**, 026 (2006) [hep-ph/0603175].
- [64] J. de Favereau *et al.* [DELPHES 3 Collaboration], JHEP **1402**, 057 (2014) [arXiv:1307.6346 [hep-ex]].
- [65] S. Chatrchyan *et al.* [CMS Collaboration], arXiv:1308.1586 [hep-ex].

- [66] S. Chatrchyan *et al.* [CMS Collaboration], JHEP **1401**, 163 (2014) [arXiv:1311.6736 [hep-ex]].
- [67] T. Aaltonen *et al.* [CDF Collaboration], Phys. Rev. Lett. **108**, 201802 (2012) [arXiv:1202.5653 [hep-ex]].
- [68] M. Czakon, P. Fiedler and A. Mitov, Phys. Rev. Lett. **110**, 252004 (2013) [arXiv:1303.6254 [hep-ph]].
- [69] N. Kidonakis, arXiv:1210.7813 [hep-ph].
- [70] K. Melnikov and F. Petriello, Phys. Rev. Lett. **96**, 231803 (2006) [hep-ph/0603182].
- [71] R. Gavin, Y. Li, F. Petriello and S. Quackenbush, Comput. Phys. Commun. **182**, 2388 (2011) [arXiv:1011.3540 [hep-ph]].
- [72] J. M. Campbell, R. K. Ellis and C. Williams, JHEP **1107**, 018 (2011) [arXiv:1105.0020 [hep-ph]].
- [73] [ATLAS Collaboration], ATLAS-CONF-2013-024.
- [74] J. Thaler and L. -T. Wang, JHEP **0807**, 092 (2008) [arXiv:0806.0023 [hep-ph]].
- [75] CMS Collaboration, CMS-PAS-JME-009-01
- [76] D. E. Kaplan, K. Rehermann, M. D. Schwartz and B. Tweedie, Phys. Rev. Lett. **101**, 142001 (2008) [arXiv:0806.0848 [hep-ph]].
- [77] T. Plehn, M. Spannowsky, M. Takeuchi and D. Zerwas, JHEP **1010**, 078 (2010) [arXiv:1006.2833 [hep-ph]].
- [78] J. Thaler and K. Van Tilburg, JHEP **1103**, 015 (2011) [arXiv:1011.2268 [hep-ph]].
- [79] J. Thaler and K. Van Tilburg, JHEP **1202**, 093 (2012) [arXiv:1108.2701 [hep-ph]].